

Supporting Information:

Influence of counterion structure on conductivity of polymerized ionic liquids

Jordan R. Keith,[†] Nathan J. Rebello,[†] Benjamin J. Cowen,[‡] and Venkat
Ganesan^{*,†}

[†]*Department of Chemical Engineering, University of Texas at Austin, Austin, Texas 78712,
United States.*

[‡]*Sandia National Laboratories, Albuquerque, New Mexico, 87185, United States*

E-mail: venkat@che.utexas.edu

S1 Simulation approach

S1.1 Use of vacuum-phase partial charges in a non-polarizable force field

In our studies, we opted to adopt vacuum-phase partial charges with a non-polarizable force field (FF) in lieu of fully polarizable FFs. Dommert et al. reviewed techniques for molecular dynamics (MD) modeling of ionic liquids (ILs), including the use of polarizable FFs or non-polarizable FFs with constant scaled partial charges.^{S1} Although polarizable FFs have been used successfully to compute transport properties, they are computationally expensive.

This issue is magnified in modeling polymerized ionic liquids (polyILs) due to slow relaxation. Morrow and Maginn were the first to investigate reduced partial charges on an IL. Using electronic structure calculations, each ion from the ion pair $\text{BmIm}^+\text{-PF}_6^-$ was assigned a total charge of ± 0.904 .^{S2} They commented that the change did not yield improvement in the static properties under consideration, but future studies revealed improvements to dynamic properties such as diffusivity.^{S3-S8} Bhargava and Balasubramanian reported accurate densities and low deviations from experimental diffusivities using a uniform scaling factor of 0.8 on vacuum-phase partial charges (VPCs) for $\text{BmIm}^+\text{-PF}_6^-$.^{S3} Zhang and Maginn also reported accurate diffusivities for $\text{BmIm}^+\text{-PF}_6^-$ ILs with the same scaling factor.^{S6} Our past work on polyILs extended the use of this same scaling approach and parameter.^{S9-S11}

Simulation studies on transport properties in ILs with other counterions lend similar support to VPC scaling. Chaban et al. determined that uniform scaling of VPCs for $\text{BmIm}^+\text{-BF}_4^-$ ILs accurately reproduced experimental diffusivities and densities with a scaling constant of 0.807.^{S5} Sprenger et al. reported diffusivity errors of 11.0% (BmIm^+) and 18.7% (TFSI^-) using the uniform scaling factor of 0.8 for VPCs.^{S7} In an earlier work on an imidazolium-series of cations with TFSI^- , Liu and Maginn showed similar agreement with experimental results for the same VPC scaling factor.^{S4} Later, Zhang and Maginn demonstrated the applicability of the uniform VPC scaling constant 0.8 to 29 ILs containing 4 distinct anions (including TFSI^- and PF_6^-) with a series of imidazolium-based cations.^{S8}

Taking the above body of work into consideration, we elected to use VPCs, scaled by 0.8, with a non-polarizable FF. We optimized molecular geometry using the B3LYP hybrid functional and 6-31G basis set in Gaussian 16.^{S12} The output was used to evaluate the electrostatic potential (ESP) at Merz-Singh-Kollman points using the Hartree-Fock level of theory with a 6-31G* basis set.^{S13,S14} The molecular ESP was fed to the restrained ESP program in Amber Antechamber to collect the atom-centered VPCs.^{S15,S16}

S1.2 Simulation details

Our earlier studies demonstrated that 16-monomer-pBvIm⁺ has a similar hexafluorophosphate (PF₆⁻) diffusivity as one of 32-monomers.^{S9,S10} Therefore, to reduce reliance on large system sizes to avoid significant polymer self-interaction, we selected a polymer length of 16 monomers for this study. We packed polyIL simulation boxes with 16 polymers and the accompanying 256 counterions using Packmol.^{S17} Similarly, IL simulations were packed with 256 ions each of BmIm⁺ and counterions. Each box was packed at a density of 0.01 g/cm³ and energy minimized via steepest-decent (SD) and conjugate-gradient (CG) minimization with a tolerance of 1×10^{-5} . The system was heated to 1000 K and compressed to 1 atm over one million timesteps of 0.01 fs using a Langevin thermostat and Berendsen barostat, both damped to relax over 100 fs.^{S18,S19} We performed MD simulations in this framework using a constant temperature/energy algorithm that limits the distance atoms can migrate over one timestep to 1.0 Å (NVE/limit). We continued initializing the system using a second SD and CG minimization to 1×10^{-5} tolerance, followed by 100 ps of simulation time at constant volume/temperature (1000 K) using a Langevin NVT simulation in the same NVE/limit framework. Initialization was concluded by cooling the simulation to the highest production temperature (600 K) and equilibrating the system briefly using a Langevin NVT simulation for 1 ns.

As indicated in the main report, all simulations in this work were performed using the LAMMPS MD software package.^{S20} Lennard-Jones (LJ) pair interactions were directly computed up to a cutoff of 10 Å. A Van der Waals tail correction to the pressure and energy were applied in a constant temperature/pressure (NPT) framework.^{S21} Coulombic interactions were directly evaluated up to the same cutoff. Long-range Coulombic interactions were evaluated using a particle-particle particle-mesh (PPPM) solver with a tolerance of 1×10^{-5} .^{S22,S23} NPT simulations were performed with a Nosé-Hoover thermostat and Parinello-Rahman barostat, adjusting temperature every 0.1 ps and pressure every 1.0 ps.^{S24-S27} Forces and

positions were evaluated with periodic boundary conditions at a regular time interval of 1.0 fs. We equilibrated ILs for 5 ns and polyILs for 10 ns using NPT simulations. After 40-80 ns of production run time, we branched the simulation to the next-lower temperature level, repeating the cooling and equilibration procedure before commencing production.

S1.3 Potential and parameters

The potential energy takes the form

$$U = \sum_r U_{bond}(r) + \sum_\theta U_{ang}(\theta) + \sum_\phi U_{dih}(\phi) + \sum_\phi U_{imp}(\phi) + \sum_{ij} U_{nb}(r_{ij}). \quad (S1)$$

where bond and angle interactions are given as harmonics, $U_{bond}(r) = k_r(r - r_0)^2$ and $U_{ang}(\theta) = k_\theta(\theta - \theta_0)^2$, with spring constants k_r and k_θ and equilibrium bond length r_0 and angle θ_0 . The energy contribution from dihedral angles is modeled using the OPLS-style dihedral potential in LAMMPS MD software:

$$U_{dih}(\phi) = \frac{1}{2} \sum_{n=1}^4 K_n [1 + (-1)^{n+1} \cos(n\phi)]. \quad (S2)$$

The energy contribution of all improper angles in which the centered atom is part of the imidazolium ring is represented by the CVFF improper style in LAMMPS, $U_{imp}(\phi) = 1.1[1 - \cos(2\phi)]$. Non-bonded interactions include LJ (6-12) pair potentials and Coulombic interactions.

$$U_{nb}(r_{ij}) = 4\epsilon_{ij} \left[\left(\frac{\sigma_{ij}}{r} \right)^{12} - \left(\frac{\sigma_{ij}}{r} \right)^6 \right] + \frac{Cq_i q_j}{r} \quad (S3)$$

The LJ parameters for pair ij include the potential-well depth ϵ_{ij} and the LJ-radius σ_{ij} , with cross terms calculated using a geometric mixing rule such that $\epsilon_{ij} = \sqrt{\epsilon_i \epsilon_j}$ and $\sigma_{ij} = \sqrt{\sigma_i \sigma_j}$. The Coulombic parameters include the partial atomic charges q_i and q_j in elementary units of charge and a constant $C = 5.514 \times 10^{-22}$ kcal-Å/e².

Table S1: Lennard-Jones parameters and unscaled partial charges for pBvIm⁺.

#	Atom Type	ϵ_{ij} (kcal/mol)	σ_{ij} (Å)	q (e)
1	CA ^{S9,S10,S28,S29}	0.0660	3.5000	-0.071916
2	CM ^{S9,S10,S28,S29}	0.0660	3.5000	-0.191281
3	CM1 ^{S9,S10,S28,S29}	0.0660	3.5000	-0.286559
4	CM2 ^{S9,S10,S28,S29}	0.0660	3.5000	-0.286559
5	CR ^{S9,S10,S28,S29}	0.0700	3.5500	-0.081640
6	CS1 ^{S9,S10,S28,S29}	0.0660	3.5000	-0.112314
7	CS2 ^{S9,S10,S28,S29}	0.0660	3.5000	0.058799
8	CT ^{S9,S10,S28,S29}	0.0660	3.5000	-0.168031
9	CW1 ^{S9,S10,S28,S29}	0.0700	3.5500	-0.203382
10	CW2 ^{S9,S10,S28,S29}	0.0700	3.5500	-0.165764
11	HA ^{S3,S9,S10}	0.0300	1.9200	0.103288
12	HM ^{S3,S9,S10}	0.0300	1.9200	0.200553
13	HM1 ^{S9,S10,S28,S29}	0.0300	2.5000	0.198717
14	HM2 ^{S9,S10,S28,S29}	0.0300	2.5000	0.132478
15	HM3 ^{S9,S10,S28,S29}	0.0300	2.5000	0.0955197
16	HR ^{S3,S9,S10}	0.0300	1.7200	0.215218
17	HS1 ^{S9,S10,S28,S29}	0.0300	2.5000	0.063370
18	HS2 ^{S9,S10,S28,S29}	0.0300	2.5000	0.032434
19	HTp ^{S9,S10,S28,S29}	0.0300	2.5000	0.056042
20	HW1 ^{S3,S9,S10}	0.0300	1.7200	0.238040
21	HW2 ^{S3,S9,S10}	0.0300	1.7200	0.244756
22	NA1 ^{S9,S10,S28,S29}	0.1700	3.2500	0.276722
23	NA2 ^{S9,S10,S28,S29}	0.1700	3.2500	0.083055

Table S2: Lennard-Jones parameters and unscaled partial charges for BmIm⁺.

#	Atom Type	ϵ_{lj} (kcal/mol)	σ_{lj} (Å)	q (e)
1	iCA ^{S9,S28,S29}	0.0660	3.5000	-0.030881
2	iCA1 ^{S9,S28,S29}	0.0660	3.5000	-0.329108
3	iCR ^{S9,S28,S29}	0.0700	3.5500	-0.022182
4	iCS1 ^{S9,S28,S29}	0.0660	3.5000	-0.128892
5	iCS2 ^{S9,S28,S29}	0.0660	3.5000	0.100350
6	iCTp ^{S9,S28,S29}	0.0660	3.5000	-0.184348
7	iCW1 ^{S9,S28,S29}	0.0700	3.5500	-0.195821
8	iCW2 ^{S9,S28,S29}	0.0700	3.5500	-0.197567
9	iHA ^{S3,S9}	0.0300	1.9200	0.094969
10	iHA1 ^{S3,S9}	0.0300	1.9200	0.168850
11	iHR ^{S3,S9}	0.0300	1.7200	0.248762
12	iHS1 ^{S9,S28,S29}	0.0300	2.5000	0.062725
13	iHS2 ^{S9,S28,S29}	0.0300	2.5000	0.019080
14	iHT ^{S9,S28,S29}	0.0300	2.5000	0.055493
15	iHW1 ^{S3,S9}	0.0300	1.7200	0.272430
16	iHW2 ^{S3,S9}	0.0300	1.7200	0.257408
17	iNA1 ^{S9,S28,S29}	0.1700	3.2500	0.024790
18	iNA2 ^{S9,S28,S29}	0.1700	3.2500	0.158482

Table S3: Lennard-Jones parameters and unscaled partial charges for AlCl_4^- (1-2), BF_4^- (3-4), Br^- (5), Cl^- (6), TfO^- (7-10), TFSI^- (11-15), PFO^- (16-21), and PFSI^- (22-28).

#	Atom Type	ϵ_{lj} (kcal/mol)	σ_{lj} (Å)	q (e)
1	Al^{S30}	0.3100	3.9111	0.837890
2	ClA^{S30}	0.2650	3.4709	-0.459473
3	$\text{B}^{\text{S29,S30}}$	0.0950	3.5814	0.889082
4	$\text{FB}^{\text{S29,S30}}$	0.0600	3.1181	-0.472250
5	Br^{S31}	0.1300	4.6200	-1.000000
6	Cl^{S32}	0.14818	3.7700	-1.000000
7	CT^{S33}	0.0660	3.5000	0.306729
8	FT^{S33}	0.0530	2.9500	-0.148380
9	OT^{S33}	0.2100	2.9600	-0.561670
10	ST^{S33}	0.2500	3.5500	0.823419
11	CF^{S33}	0.0660	3.5000	0.398201
12	FF^{S33}	0.0530	2.9500	-0.140678
13	NF^{S33}	0.1700	3.2500	-0.545246
14	OF^{S33}	0.2100	2.9600	-0.516122
15	SF^{S33}	0.2500	3.55000	0.828700
16	CN1^7	0.0660	3.5000	0.153764
17	CN2^7	0.0660	3.5000	0.511147
18	FN1^8	0.0530	2.9500	-0.153290
19	FN2^8	0.0530	2.9500	-0.179270
20	ON^9	0.2100	2.9600	-0.554590
21	SN^{10}	0.2500	3.5500	0.843253
22	CP1^{S33}	0.0660	3.5000	0.199513
23	CP2^{22}	0.0660	3.5000	0.557018
24	FP1^{S33}	0.0530	2.9500	-0.140303
25	FP2^{24}	0.0530	2.9500	-0.181706
26	NP^{S33}	0.1700	3.2500	-0.526543
27	OP^{S33}	0.2100	2.9600	-0.510183
28	SP^{S33}	0.2500	3.55000	0.852830

Table S4: Harmonic bond parameters for pBvIm⁺.

#	Bond Type	k_r (kcal/mol-Å ²)	r_0 (Å)
1	CA-CS1 ^{S9}	280.159	1.534
2	CA-HA ^{S9}	357.723	1.092
3	CA-NA2 ^{S9}	287.313	1.478
4	CM-CM1 ^{S9}	276.101	1.532
5	CM-CM2 ^{S9}	276.101	1.532
6	CM-HM ^{S9}	363.651	1.083
7	CM-NA1 ^{S9}	274.189	1.486
8	CM1-HM1 ^{S9}	348.875	1.095
9	CM2-HM2 ^{S9}	348.875	1.095
10	CM2-HM3 ^{S9}	348.875	1.095
11	CR-HR ^{S9}	401.204	1.074
12	CR-NA1 ^{S9}	464.417	1.385
13	CR-NA2 ^{S9}	552.388	1.335
14	CS1-CS2 ^{S9}	281.515	1.536
15	CS1-HS1 ^{S9}	347.494	1.091
16	CS2-CTp ^{S9}	287.616	1.532
17	CS2-HS2 ^{S9}	349.100	1.095
18	CTp-HT ^{S9}	351.780	1.093
19	CW1-CW2 ^{S9}	531.524	1.352
20	CW1-HW1 ^{S9}	396.395	1.081
21	CW1-NA1 ^{S9}	410.333	1.386
22	CW2-HW2 ^{S9}	395.457	1.079
23	CW2-NA2 ^{S9}	408.436	1.384

Table S5: Harmonic bond parameters for BmIm⁺.

#	Bond Type	k_r (kcal/mol-Å ²)	r_0 (Å)
1	iCA-iCS1 ^{S9}	280.159	1.534
2	iCA-iHA ^{S9}	357.723	1.092
3	iCA1-iHA1 ^{S9}	357.723	1.092
4	iCA-iNA2 ^{S9}	287.313	1.478
5	iCA1-iNA1 ^{S9}	287.313	1.478
6	iCR-iHR ^{S9}	401.204	1.074
7	iCR-iNA1 ^{S9}	464.417	1.385
8	iCR-iNA2 ^{S9}	552.388	1.335
9	iCS1-iCS2 ^{S9}	281.515	1.536
10	iCS1-iHS1 ^{S9}	347.494	1.091
11	iCS2-iCTp ^{S9}	287.616	1.532
12	iCS2-iHS2 ^{S9}	349.100	1.095
13	iCTp-iHT ^{S9}	351.780	1.093
14	iCW1-iCW2 ^{S9}	531.524	1.352
15	iCW1-iHW1 ^{S9}	396.395	1.081
16	iCW1-iNA1 ^{S9}	410.333	1.386
17	iCW2-iHW2 ^{S9}	395.457	1.079
18	iCW2-iNA2 ^{S9}	408.436	1.384

Table S6: Harmonic bond parameters for AlCl_4^- (1), BF_4^- (2), TfO^- (3-5), TFSI^- (6-9), PFO^- (10-14), and PFSI^- (15-20).

#	Bond Type	k_r (kcal/mol-Å ²)	r_0 (Å)
1	Al-ClA ^{S30}	116.000	2.170
2	B-FB ^{S30}	290.000	1.393
3	CT-FT ^{S33}	441.800	1.323
4	CT-ST ^{S33}	235.400	1.818
5	ST-OT ^{S33}	637.100	1.442
6	CF-FF ^{S33}	441.800	1.323
7	CF-SF ^{S33}	235.400	1.818
8	NF-SF ^{S33}	372.000	1.570
9	SF-OF ^{S33}	637.100	1.442
10	CN1-FN1 ^{S33}	441.800	1.323
11	CN2-FN2 ¹⁰	441.800	1.323
12	CN1-SN ^{S33}	235.400	1.818
13	SN-ON ^{S33}	637.100	1.442
14	CN1-CN2 ²⁰	134.000	1.529
15	CP1-FP1 ^{S34}	442.000	1.340
16	CP2-FP2 ¹⁵	442.000	1.340
17	CP1-SP ^{S34}	235.500	1.835
18	NP-SP ^{S34}	372.000	1.600
19	SP-OP ^{S34}	637.000	1.450
20	CP1-CP2 ^{S34}	134.000	1.529

S1.4 Commentary on the temperature range and implications for real materials

Green et al. reports the degradation temperatures of four of the polyILs studied herein.^{S35} According to their results (“degredation” at 5% weight loss), pBvIm⁺-TFSI⁻ and -TfO⁻ are stable at and below 600 K (our highest temperature), while pBvIm⁺-BF₄⁻ degrades at 568 K and -Br⁻ at 533 K. Although not all of these materials are stable at these temperatures (nor do the experimental conductivities reported in literature extend to such high temperatures), we are confident in our choice to investigate such temperatures to keep simulation run times manageable. While there may be no material applications at these high temperatures, the insights gained into the transport mechanism will be relevant at these “unphysical” temperatures in the same way that they are at lower temperatures. However, an order of magnitude reduction in mobility, which could be expected with a temperature decrease of 50 to 100 K, would require an additional order of magnitude of run time to access the diffusive regime. Since the underlying physical insights are unlikely to diverge from those observed at the current temperature levels, we see it as imprudent to probe lower temperatures.

S2 Details of Analysis

S2.1 Measuring association distance and determining an unbiased cutoff radius

The “center” of the cations was taken to be the nitrogen labeled NA2 (polyIL) and iNA2 (IL). Likewise, we chose a single atom within each anion to represent its center: Al (AlCl₄⁻), B (BF₄⁻), Br (Br⁻), Cl (Cl⁻), SN (PfO⁻), NP (PFSI⁻), ST (TfO⁻), and NF (TFSI⁻). These atom identifiers, and all other atom identifiers (associated with the data in Tables S1-S12), can be located in Figure S1. For the spherically symmetric species and the linear

Table S7: Harmonic angle parameters for pBvIm⁺. *Units kcal/mol-rad²

#	Cent Atom	Outer Atoms	k_θ^*	θ_0 (deg)
1	CA	CS1-HA ^{S9}	63.034	111.966
2	CA	CS1-NA2 ^{S9}	78.829	112.124
3	CA	HA-HA ^{S9}	63.013	107.853
4	CA	HA-NA2 ^{S9}	71.809	106.307
5	CM	CM1-CM1 ^{S9}	86.605	113.354
6	CM	CM1-CM2 ^{S9}	86.605	113.354
7	CM	CM1-HM ^{S9}	62.36	109.018
8	CM	CM1-NA1 ^{S9}	100.742	109.948
9	CM	CM2-HM ^{S9}	62.36	109.018
10	CM	CM2-NA1 ^{S9}	100.742	109.948
11	CM	HM-NA1 ^{S9}	81.775	104.182
12	CM1	CM-CM ^{S9}	93.377	116.755
13	CM1	CM-HM1 ^{S9}	65.863	109.352
14	CM1	HM1-HM1 ^{S9}	54.233	108.068
15	CM2	CM-HM2 ^{S9}	65.863	109.352
16	CM2	CM-HM3 ^{S9}	65.863	109.352
17	CM2	HM2-HM2 ^{S9}	54.233	108.068
18	CM2	HM3-HM3 ^{S9}	54.233	108.068
19	CR	HR-NA1 ^{S9}	64.617	125.669
20	CR	HR-NA2 ^{S9}	66.082	125.132
21	CR	NA1-NA2 ^{S9}	252.744	109.164
22	CS1	CA-CS2 ^{S9}	80.939	112.443
23	CS1	CA-HS1 ^{S9}	67.208	109.146
24	CS1	CS2-HS1 ^{S9}	55.219	108.941
25	CS1	HS1-HS1 ^{S9}	56.563	107.458
26	CS2	CS1-CTp ^{S9}	80.4	114.212
27	CS2	CS1-HS2 ^{S9}	59.461	107.908
28	CS2	CTp-HS2 ^{S9}	58.884	109.477
29	CS2	HS2-HS2 ^{S9}	82.095	106.005
30	CTp	CS2-HT ^{S9}	63.976	111.352
31	CTp	HT-HT ^{S9}	68.335	108.358
32	CW1	CW2-HW1 ^{S9}	58.627	130.162
33	CW1	CW2-NA1 ^{S9}	255.171	106.709
34	CW1	HW1-NA1 ^{S9}	68.306	122.79
35	CW2	CW1-HW2 ^{S9}	64.721	130.027
36	CW2	CW1-NA2 ^{S9}	268.303	107.291
37	CW2	HW2-NA2 ^{S9}	61.818	122.991
38	NA1	CM-CR ^{S9}	90.685	126.384
39	NA1	CM-CW1 ^{S9}	97.374	125.886
40	NA1	CR-CW1 ^{S9}	266.725	107.813
41	NA1	CA-CR ^{S9}	84.594	126.178
42	NA1	CA-CW2 ^{S9}	88.387	126.334
43	NA1	CR-CW2 ^{S9}	97.245	108.165

Table S8: Harmonic angle parameters for BmIm⁺. *Units kcal/mol-rad²

#	Cent Atom	Outer Atoms	k_θ^*	θ_0 (deg)
1	iCA	iCS1-iHA ^{S9}	63.034	111.966
2	iCA	iCS1-iNA2 ^{S9}	78.829	112.124
3	iCA	iHA-iHA ^{S9}	63.013	107.853
4	iCA	iHA-iNA2 ^{S9}	71.809	106.307
5	iCA1	iHA1-iHA1 ^{S9}	63.013	107.853
6	iCA1	iHA1-iNA1 ^{S9}	71.809	106.307
7	iCR	iHR-iNA1 ^{S9}	64.617	125.669
8	iCR	iHR-iNA2 ^{S9}	66.082	125.132
9	iCR	iNA1-iNA2 ^{S9}	252.74	109.164
10	iCS1	iCA-iCS2 ^{S9}	80.939	112.443
11	iCS1	iCA-iHS1 ^{S9}	67.208	109.146
12	iCS1	iCS2-iHS1 ^{S9}	55.219	108.941
13	iCS1	iHS1-iHS1 ^{S9}	56.563	107.458
14	iCS2	iCS1-iCT ^{S9}	80.4	114.212
15	iCS2	iCS1-iHS2 ^{S9}	59.461	107.908
16	iCS2	iCT-iHS2 ^{S9}	58.884	109.477
17	iCS2	iHS2-iHS2 ^{S9}	82.095	106.005
18	iCTp	iCS2-iHT ^{S9}	63.976	111.352
19	iCTp	iHT-iHT ^{S9}	68.335	108.358
20	iCW1	iCW2-iHW1 ^{S9}	58.627	130.162
21	iCW1	iCW2-iNA1 ^{S9}	255.171	106.709
22	iCW1	iHW1-iNA1 ^{S9}	68.306	122.79
23	iCW2	iCW1-iHW2 ^{S9}	64.721	130.027
24	iCW2	iCW1-iNA2 ^{S9}	268.303	107.291
25	iCW2	iHW2-iNA2 ^{S9}	61.818	122.991
26	iNA1	iCA1-iCR ^{S9}	84.594	126.178
27	iNA1	iCA1-iCW1 ^{S9}	88.387	126.334
28	iNA1	iCR-iCW1 ^{S9}	266.725	107.813
29	iNA2	iCA-iCR ^{S9}	84.594	126.178
30	iNA2	iCA-iCW2 ^{S9}	88.387	126.334
31	iNA2	iCR-iCW2 ^{S9}	97.245	108.165

Table S9: Harmonic angle parameters for AlCl_4^- (1), BF_4^- (2), TfO^- (3-6), TFSI^- (7-13), PfO^- (14-21), and PFSI^- (22-32). *Units kcal/mol-rad²

#	Cent Atom	Outer Atoms	k_θ^*	θ_0 (deg)
1	Al	ClA-ClA ^{S30}	50	109.5
2	B	FB-FB ^{S30}	50	109.5
3	ST	OT-OT ^{S33}	115.8	100.2
4	ST	CT-OT ^{S33}	104	102.6
5	CT	FT-FT ^{S33}	93.3	107.1
6	CT	ST-FT ^{S33}	83	111.8
7	SF	CF-NF ^{S33}	97.5	100.2
8	SF	CF-OF ^{S33}	104	102.6
9	CF	FF-FF ^{S33}	93.3	107.1
10	CF	SF-FF ^{S33}	83	111.8
11	SF	OF-NF ^{S33}	94.3	113.6
12	SF	OF-OF ^{S33}	115.5	118.5
13	NF	SF-SF ^{S33}	80.2	125.6
14	SN	ON-ON ^{S33}	115.8	100.2
15	SN	CN1-ON ^{S33}	104	102.6
16	CN1	FN1-FN1 ^{S33}	93.3	107.1
17	CN2	FN2-FN2 ¹⁷	93.3	107.1
18	CN1	SN-FN1 ^{S33}	83	111.8
19	CN1	CN2-SN ³⁰	50	116
20	CN1	CN2-FN1 ³¹	50	109.3
21	CN2	CN1-FN2 ³¹	50	109.3
22	SP	CP1-NP ^{S34}	97.5	100.2
23	SP	CP1-OP ^{S34}	104	102.6
24	CP1	FP1-FP1 ^{S34}	93.5	108.6
25	CP2	FP2-FP2 ²⁴	93.5	108.6
26	CP1	SP-FP1 ^{S34}	83	110.4
27	SP	OP-NP ^{S34}	94.5	111.4
28	SP	OP-OP ^{S34}	116	120.2
29	NP	SP-SP ^{S34}	40	121
30	CP1	CP2-SP ^{S34}	50	116
31	CP1	CP2-FP1 ^{S34}	50	109.3
32	CP2	CP1-FP2 ³¹	50	109.3

Table S10: OPLS dihedral parameters for pBvIm⁺. *Units kcal/mol.

#	Cent Bond	Outer Atoms	K_1^*	K_2^*	K_3^*	K_4^*
1	CA-CS1	HA-CS2 ^{S28,S29}	0	0	0.366	0
2	CA-CS1	HA-HS1 ^{S28,S29}	0	0	0.318	0
3	CA-CS1	NA2-CS2 ^{S28,S29}	-1.788	0.756	-0.288	0
4	CA-CS1	NA2-HS1 ^{S28,S29}	0	0	0	0
5	CA-NA2	CS1-CR ^{S28,S29}	-1.659	-0.555	-0.375	0
6	CA-NA2	CS1-CW2 ^{S28,S29}	-1.91	-1.5	0.29	0
7	CA-NA2	HA-CR ^{S28,S29}	0	0	0	0
8	CA-NA2	HA-CW2 ^{S28,S29}	-1.4	-2.65	0.175	0
9	CM-CM1	CM1-CM ^{S9}	-0.775803	0.313249	4.69238	0.31007
10	CM-CM1	CM1-HM1 ^{S9}	0	0	2.67777	0
11	CM-CM1	CM2-CM ^{S9}	-0.775803	0.313249	4.69238	0.31007
12	CM-CM1	CM2-HM1 ^{S9}	0	0	2.67777	0
13	CM-CM1	HM-CM ^{S9}	0	0	2.67777	0
14	CM-CM1	HM-HM1 ^{S9}	0	0	2.78174	0
15	CM-CM1	NA1-CM ^{S9}	0	0	4.44212	0
16	CM-CM1	NA1-HM1 ^{S9}	-0.839253	-0.310509	4.68038	0.846371
17	CM-CM2	CM1-HM2 ^{S9}	0	0	2.67777	0
18	CM-CM2	HM-HM2 ^{S9}	0	0	2.78174	0
19	CM-CM2	NA1-HM2 ^{S9}	-0.839253	-0.310509	4.68038	0.846371
20	CM-NA1	CM1-CR ^{S9}	2.45324	-0.559275	-0.813571	1.52831
21	CM-NA1	CM1-CW1 ^{S9}	0	0	2.37904	0
22	CM-NA1	CM2-CR ^{S9}	2.45324	-0.559275	-0.813571	1.52831
23	CM-NA1	CM2-CW1 ^{S9}	0	0	2.37904	0
24	CM-NA1	HM-CR ^{S9}	0	0	0	0
25	CM-NA1	HM-CW1 ^{S9}	0	0	0.124	0
26	CM2-CM	HM3-CM1 ^{S9}	0	0	2.67777	0
27	CM2-CM	HM3-HM ^{S9}	0	0	2.78174	0
28	CM2-CM	HM3-NA1 ^{S9}	-0.839253	-0.310509	4.68038	0.846371
29	CR-NA1	HR-CM ^{S28,S29}	0	4.651	0	0
30	CR-NA1	HR-CW1 ^{S28,S29}	0	4.651	0	0
31	CR-NA1	NA2-CM ^{S9}	0	4.651	0	0
32	CR-NA1	NA2-CW1 ^{S28,S29}	0	4.651	0	0
33	CR-NA2	HR-CA ^{S28,S29}	0	4.651	0	0
34	CR-NA2	HR-CW2 ^{S28,S29}	0	4.651	0	0
35	CR-NA2	NA1-CA ^{S28,S29}	0	4.651	0	0
36	CR-NA2	NA1-CW2 ^{S28,S29}	0	4.651	0	0
37	CS1-CS2	CA-CTp ^{S28,S29}	1.3	-0.05	0.2	0
38	CS1-CS2	CA-HS2 ^{S28,S29}	0	0	0.366	0
39	CS1-CS2	HS1-CTp ^{S28,S29}	0	0	0.366	0
40	CS1-CS2	HS1-HS2 ^{S28,S29}	0	0	0.318	0
41	CS2-CTp	CS1-HT ^{S28,S29}	0	0	0.366	0
42	CS2-CTp	HS2-HT ^{S28,S29}	0	0	0.318	0
43	CW1-CW2	HW1-HW2 ^{S28,S29}	0	10.75	0	0
44	CW1-CW2	HW1-NA2 ^{S28,S29}	0	10.75	0	0
45	CW1-CW2	NA1-HW2 ^{S28,S29}	0	10.75	0	0
46	CW1-CW2	NA1-NA2 ^{S28,S29}	0	10.75	0	0
47	CW1-NA1	CW2-CM ^{S9}	0	3	0	0
48	CW1-NA1	CW2-CR ^{S28,S29}	0	3	0	0
49	CW1-NA1	HW1-CM ^{S9}	0	3	0	0
50	CW1-NA1	HW1-CR ^{S28,S29}	0	3	0	0
51	CW2-NA2	CW1-CA ^{S28,S29}	0	3	0	0
52	CW2-NA2	CW1-CR ^{S28,S29}	0	3	0	0
53	CW2-NA2	HW2-CA ^{S28,S29}	0	3	0	0
54	CW2-NA2	HW2-CR ^{S28,S29}	0	3	0	0

Table S11: OPLS dihedral parameters for BmIm⁺. *Units kcal/mol.

#	Cent Bond	Outer Atoms	K_1^*	K_2^*	K_3^*	K_4^*
1	iCA-iCS1	iHA-iCS2 ^{S28,S29}	0	0	0.366	0
2	iCA-iCS1	iHA-iHS1 ^{S28,S29}	0	0	0.318	0
3	iCA-iCS1	iNA2-iCS2 ^{S28,S29}	-1.788	0.756	-0.288	0
4	iCA-iCS1	iNA2-iHS1 ^{S28,S29}	0	0	0	0
5	iCA-iNA2	iCS1-iCR ^{S28,S29}	-1.659	-0.555	-0.375	0
6	iCA-iNA2	iCS1-iCW2 ^{S28,S29}	-1.91	-1.5	0.29	0
7	iCA-iNA2	iHA-iCR ^{S28,S29}	0	0	0	0
8	iCA-iNA2	iHA-iCW2 ^{S28,S29}	-1.4	-2.65	0.175	0
9	iCR-iNA1	iHR-iCW1 ^{S28,S29}	0	4.651	0	0
10	iCR-iNA1	iNA2-iCW1 ^{S28,S29}	0	4.651	0	0
11	iCR-iNA2	iHR-iCA ^{S28,S29}	0	4.651	0	0
12	iCR-iNA2	iHR-iCW2 ^{S28,S29}	0	4.651	0	0
13	iCR-iNA2	iNA1-iCA ^{S28,S29}	0	4.651	0	0
14	iCR-iNA2	iNA1-iCW2 ^{S28,S29}	0	4.651	0	0
15	iCS1-iCS2	iCA-iCTp ^{S28,S29}	1.3	-0.05	0.2	0
16	iCS1-iCS2	iCA-iHS2 ^{S28,S29}	0	0	0.366	0
17	iCS1-iCS2	iHS1-iCTp ^{S28,S29}	0	0	0.366	0
18	iCS1-iCS2	iHS1-iHS2 ^{S28,S29}	0	0	0.318	0
19	iCS2-iCTp	iCS1-iHT ^{S28,S29}	0	0	0.366	0
20	iCS2-iCTp	iHS2-iHT ^{S28,S29}	0	0	0.318	0
21	iCW1-iCW2	iHW1-iHW2 ^{S28,S29}	0	10.75	0	0
22	iCW1-iCW2	iHW1-iNA2 ^{S28,S29}	0	10.75	0	0
23	iCW1-iCW2	iNA1-iHW2 ^{S28,S29}	0	10.75	0	0
24	iCW1-iCW2	iNA1-iNA2 ^{S28,S29}	0	10.75	0	0
25	iCW1-iNA1	iCW2-iCR ^{S28,S29}	0	3	0	0
26	iCW1-iNA1	iHW1-iCR ^{S28,S29}	0	3	0	0
27	iCW2-iNA2	iCW1-iCA ^{S28,S29}	0	3	0	0
28	iCW2-iNA2	iCW1-iCR ^{S28,S29}	0	3	0	0
29	iCW2-iNA2	iHW2-iCA ^{S28,S29}	0	3	0	0
30	iCW2-iNA2	iHW2-iCR ^{S28,S29}	0	3	0	0
31	iNA1-iCR	iCA1-iNA2 ^{S28,S29}	0	4.651	0	0
32	iNA1-iCR	iCA1-iHR ^{S28,S29}	0	4.651	0	0
33	iCW1-iNA1	iCW2-iCA1 ^{S28,S29}	0	3	0	0
34	iCW1-iNA1	iHW1-iCA1 ^{S28,S29}	0	3	0	0
35	iCA1-iNA1	iHA1-iCR ^{S28,S29}	0	0	0	0
36	iCA1-iNA1	iHA1-iCW1 ^{S28,S29}	-1.4	-2.65	0.175	0

Table S12: OPLS dihedral parameters for TfO⁻ (1), TFSI⁻ (2-5), PfO⁻ (6-9), and PFSI⁻ (10-17). *Units kcal/mol.

#	Cent Bond	Outer Atoms	K_1^*	K_2^*	K_3^*	K_4^*
1	CT-ST	FT-OT ^{S33}	0	0	0.3468	0
2	CF-SF	FF-NF ^{S33}	0	0	0.316	0
3	CF-SF	FF-OF ^{S33}	0	0	0.3468	0
4	NF-SF	SF-CF ^{S33}	7.8329	-2.4904	-0.7636	0
5	NF-SF	SF-OF ^{S33}	0	0	-0.0036	0
6	CN1-SN	FN1-ON ^{S33}	0	0	0.3468	0
7	CN1-SN	CN2-ON ¹⁴	0	0	0.347	0
8	CN2-CN1	FN2-FN1 ¹⁶	0	0	0.335	0
9	CN2-CN1	FN2-SN ¹⁷	0	0	0	0
10	CP1-SP	FP1-NP ^{S34}	0	0	0	0
11	CP1-SP	FP1-OP ^{S34}	0	0	0.171	0
12	NP-SP	SP-CP1 ^{S34}	7.833	2.49	-0.764	0
13	NP-SP	SP-OP ^{S34}	0	0	-0.0036	0
14	CP1-SP	CP2-OP ^{S34}	0	0	0.347	0
15	CP1-SP	CP2-NP ^{S34}	-0.288	1.247	-0.635	0
16	CP2-CP1	FP2-FP1 ^{S34}	0	0	0.335	0
17	CP2-CP1	FP2-SP ^{S34}	0	0	0	0

asymmetric TfO⁻ and PfO⁻, the choices could be naturally tied to the distributed charge geometry, focusing attention on the region of concentrated negative charge. For TFSI⁻ and PFSI⁻, although the nitrogen does not reflect a charge-centered atom, it was selected to ensure that only one atom represented each anion, and that the proposed center would not reside where the association distance could be nonphysically close to zero. All hydrogen atoms in the BmIm⁺ and pBvIm⁺ are left out of this figure to improve its clarity. Hydrogen atoms are named to mirror the carbon atom to which they are connected. For example, the hydrogen atoms bonded to CA are named HA. Likewise, those bonded to iCA are named iHA. All anion atoms are explicitly labeled.

The cutoff distance is a critical quantity in a number of our analysis methods, including the intermittent ion-association auto-correlation function ($C(t)$), continuous ion-association auto-correlation function ($S(t)$), coordination profile, and ion hopping frequencies. $C(t)$ was

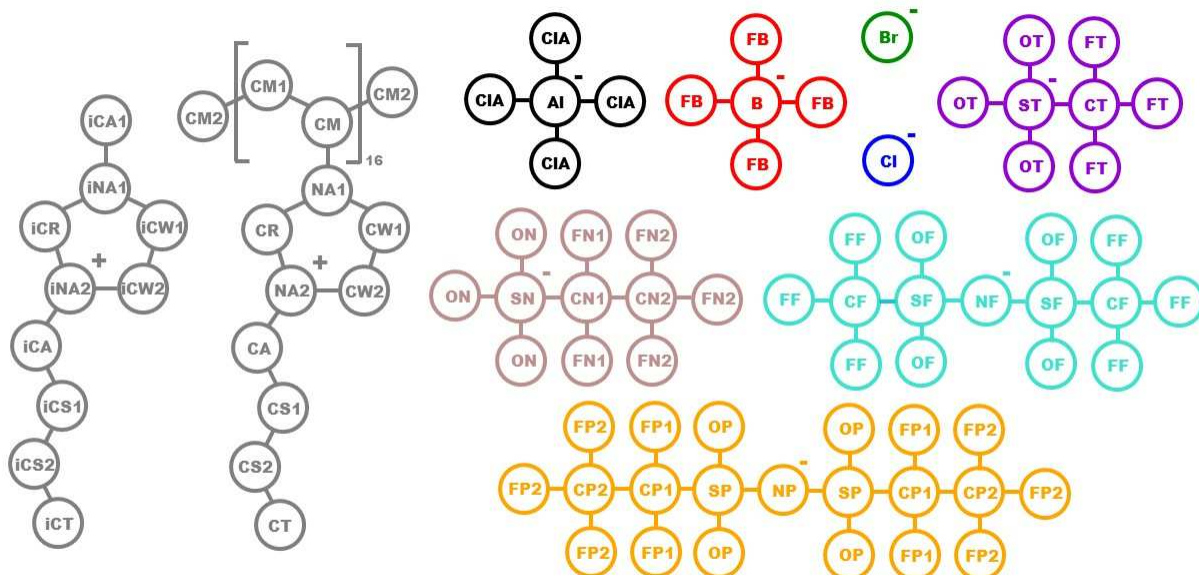


Figure S1: Mapping for all ions and polymers included in this study. The names shown above correspond to those used in the tables for potential parameters, including non-bonded, bond, angle, and dihedral energies. The positive- or negative-charged label indicates the cation or anion center atom chosen to represent the ion in coordination and association studies. Hydrogen atoms are left out for improved clarity. Naming convention for hydrogen atoms mirrors that for their connected carbon atoms. Ions are as follows, from upper left to lower right: BmIm⁺ (grey), pBvIm⁺ (grey), AlCl₄⁻ (black), BF₄⁻ (red), Br⁻ (green), TfO⁻ (violet), Cl⁻ (blue), PfO⁻ (brown), TFSI⁻ (turquoise), and PF₆⁻ (orange).

discussed at length in the main article, and the rest will be addressed throughout SI. Previously, we utilized a constant, arbitrarily chosen cutoff for the single anion type investigated in atomistic molecular dynamics simulations of polyILs, PF_6^- .^{S9-S11} Now, confronted with varying physicochemical characteristics for each ion, a consistent, universal definition based on the radial distribution function ($g(r)$) must be adopted. The choice is the distance at which $g(r) = 1$ on the negative slope of the first coordination peak. We will refer to such a distance as the radius of ionic *association*, which should not be confused with the radius for ion *pairing*. Ion pairing distance is better represented by the radius at which the average coordination number reaches 1.0. Figure S2 shows these distances, along with the radius of

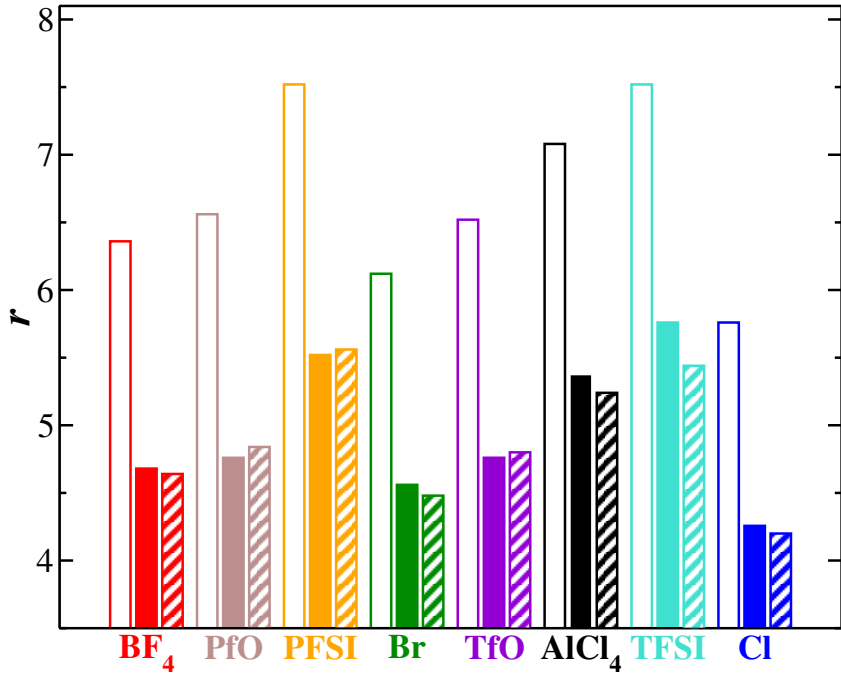


Figure S2: Open symbols are cutoff distance based on the entire first peak of the radial distribution function ($g(r)$). Solid filled symbols represent the radius at which the first maximum in the radial distribution function is observed. The patterned symbols show the radius at which the average coordination number is 1.0 (ion-pair cutoff distance). The ions are presented left to right in order of conductivity/dynamics-decoupling extent from the main article.

the maximum in the first peak of the $g(r)$. For the spherical ions and TFSI^- , the maximum

peak falls beyond the ion-pair distance. This suggests that multiple anions can be closely *associated* to a single cation. This is an important distinction, as we are purposely using *associated* rather than *bound* to avoid implying that ions require higher energy to escape association. This detail will emerge later in our analysis. To conclude this point, the maximum peaks for PfO^- , TfO^- , and PFSI^- lie inside of the respective ion-pair cutoff, implying that not all cations have a closely associated counterpart. It is worth noting the disparity between the first-peak radius and the ion-pair radius in TFSI^- , and to a lesser extent, AlCl_4^- . These two species emerge as key, highly decoupled species in the main article, and within the SI, we devote some attention to analyzing the underlying origins. Finally, the overall trends in the solid-filled and pattern-filled in Figure S2 follow the trend of the association cutoff distance (open symbols). PFSI^- and TFSI^- have similar distances, as do PfO^- and TfO^- . AlCl_4^- falls between these two sets, while the remaining spherical species lie below the rest, with the distances directly proportional to the ionic radius.

S2.2 Determining glass-transition temperatures from simulation

We determined the glass-transition temperatures (T_g) for all of the polyIL materials (Figure S5) and IL materials (Figure S3) evaluated in this study. We used the volumetric expansion method by quantifying density as a function of temperature. For ILs, fast structural relaxation allows the materials to equilibrate quickly, thus enabling the use of a rapid cooling rate of 5 K/ns. Beginning with a well-equilibrated configuration at 450 K, we continuously and linearly cooled the sample to 100 K for 100 ns of simulation time. We used the NPT ensemble using the same strategies employed for the production and equilibration procedure, described in Section S1.2. Figure S3 summarizes the results, along with the fitting lines for both high- (red) and low-temperature (blue) regions of the density curve. The green dotted line on each graph draws the readers attention to the intersection point of the two fitting lines. The value of temperature at these intersections represents T_g , and the IL T_g s are

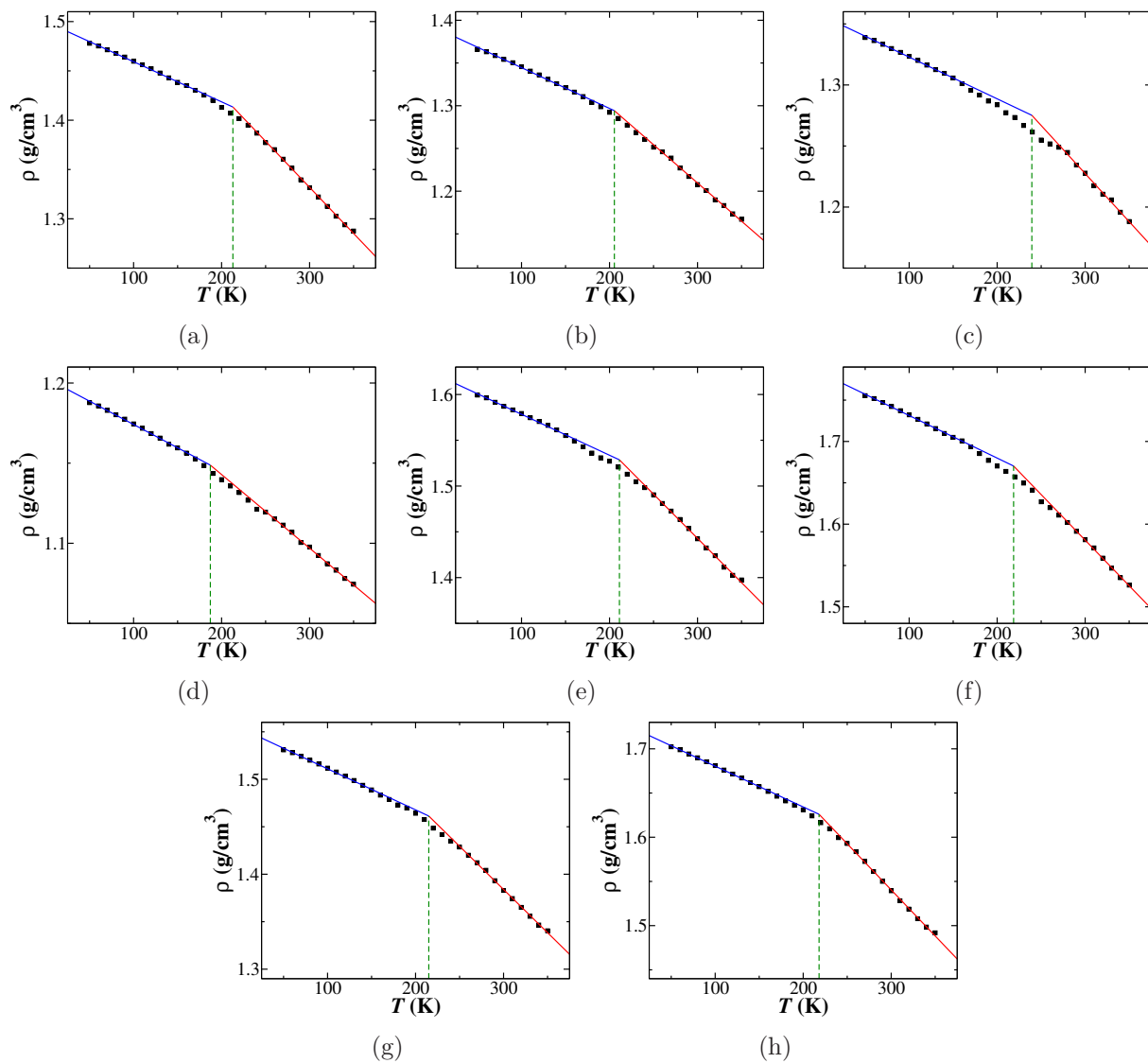


Figure S3: Plots of density versus temperature for ionic liquid (IL) materials. BmIm⁺ with counterions: a) AlCl₄⁻, b) BF₄⁻, c) Br⁻, d) Cl⁻, e) PfO⁻, f) PFSI⁻, g) TfO⁻, h) TFSI⁻.

reported in Table S13 in column 2.

Table S13: Values of T_g extracted from the intersection of lines fit above and below T_g on density versus temperature plots.

anion	T_{gIL}	$T_{gpolyIL}$
AlCl_4^-	213	231
BF_4^-	205	185
Br^-	239	222
Cl^-	187	305
PfO^-	211	227
PFSI^-	219	232
TfO^-	215	237
TFSI^-	218	260

The T_g s for polyILs were more difficult to extract. PolyILs relax at a much slower rate, causing uncertainty in the values of density extracted from rapid cooling simulations, such as the ones executed for the IL materials. Furthermore, the range of possible values for T_g was extensive upon initial inspection. Many early attempts were made to characterize T_g using prior knowledge of experimental values for these materials. T_g is known from experiment for five of the eight polyILs tested in this study, and an empirical fit between the molecular volume of the ion pair and T_g , proposed by Bocharova et al., provided an estimate of the unknown T_g s.^{S36} The empirical formula is as follows,

$$\frac{1}{T_{g0}} = \left(A + \frac{B}{V_m^{1/3}} + CV_m^{2/3} \right)^{-1} - \frac{K}{V_m}, \quad (\text{S4})$$

where T_{g0} represents the T_g of an infinitely long polymer. This equation includes the term containing a fourth adjustable parameter (K), which reflects the influence of variable molecular weight, described and cited to Ueberreiter and Kanig by Bocharova et al.^{S36,S37} Figure S4 summarizes this information, and a number of sources are credited with these experimental results, while differing values are averaged to the value shown on this plot.^{S35,S38,S39} Molecular volume measurements were compiled from a number of other sources, with some results,

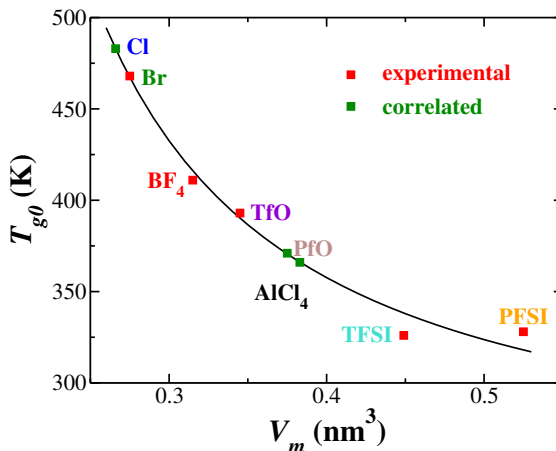


Figure S4: Experimental and empirically derived infinite-length-polymer T_g for all polyILs tested in this study.

specifically for some fluorinated ionic species and the polyIL backbone atoms, being derived from group-contribution volume estimating.^{S40–S43} Given that such values represent the dynamics of infinitely long polymers, it is reasonable to assume that the lower molecular weight tested in this study will lead to lower T_g . Our search space initially included 250 K to 600 K, depending on the material and the expected value of T_g . We tried the same procedure used with success on the ILs for these ranges at cooling rates of 5 K/ns, 1 K/ns, and 0.4 K/ns. In all cases, we failed to isolate a repeatable and identifiable transition.

The FF parameters utilized in this study are not validated against experimental properties such as density in the polyILs. Nor are the molecular volumes, derived from experiment, necessarily representative of such values in the simulation environment. Thus, we cannot be certain that these materials will follow the same trends identified in real materials. This makes it crucial to extract T_g from simulations. In a final attempt to extract T_g , we used NPT simulations with 100 ns of equilibration time and 50 ns of production data collection to compute the average density at over intervals of 25 K from 25 to 650 K. Figure S5 shows the results of this procedure. We are encouraged by the obvious change in slope that occurs near the T_g for each material. Values were extracted using the same procedure described for

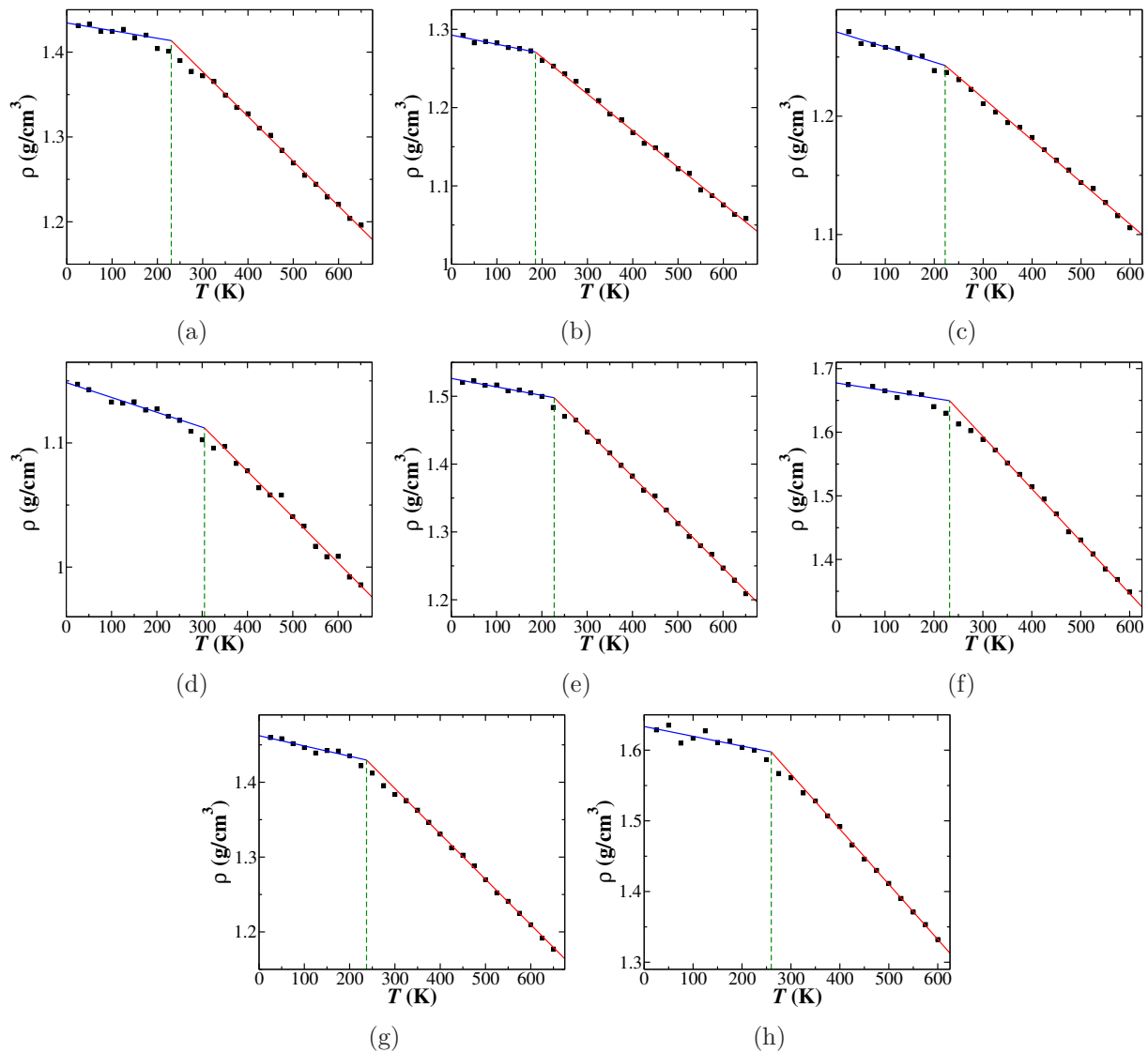


Figure S5: Plots of density versus temperature for polyIL materials. pBvIm⁺ with counterions: a) AlCl₄⁻, b) BF₄⁻, c) Br⁻, d) Cl⁻, e) PfO⁻, f) PFSI⁻, g) TfO⁻, h) TFSI⁻.

ILs and are included in column 3 of Table S13 for the reader’s convenience. These values are surprisingly low, given the experimental values shown previously. Even the trend is seen to differ from the experimental results. We speculate that the use of empirically charge scaled force fields to be a potential origin for such discrepancies.

S2.3 Commentary on conductivity and glass-transition temperature, and their impacts on observed decoupling outcomes

Figure S6(a) shows the raw conductivities reported as a function of inverse temperature. We see that pBvIm⁺-BF₄⁻ and -TfO⁻ approach their experimental counterparts, although they were tested at slightly higher temperatures than in experiment. Since the temperature range does not overlap, we cannot be sure that the slope seen for the simulation study matches that of the real material. As for the pBvIm⁺-TFSI⁻ and -PFSI⁻, the simulation conductivities appear to be lower than those expected from experiments. The pBvIm⁺-TFSI⁻ simulation curve has a partial overlap with the highest temperatures probed by experiment. The slope appears to be less negative for the simulation data, but the difference does not appear to be great in the range considered.

Since the computed conductivities do not depart greatly from the experimental results, we expect that the calculated T_g will drive any departures of the degree of decoupling between this study and experiment. Indeed, we do see a difference in the order of decoupling from Figure S6(b). For the experimental studies: BF₄⁻ > TFSI⁻ > TfO⁻ > PFSI⁻. Namely, BF₄⁻ is the most decoupled in the experimental studies, but is the least decoupled in our study. This arises from the low T_g computed for pBvIm⁺-BF₄⁻, which is inconsistent with the trend in T_g reported experimentally. By adjusting the value of T_g from that of simulation to that of the experiment in Figure S6(c), we see that pBvIm⁺-BF₄⁻ lies in the correct relative position, but that -TFSI⁻ lies out of order. This would undoubtedly be attributed to the

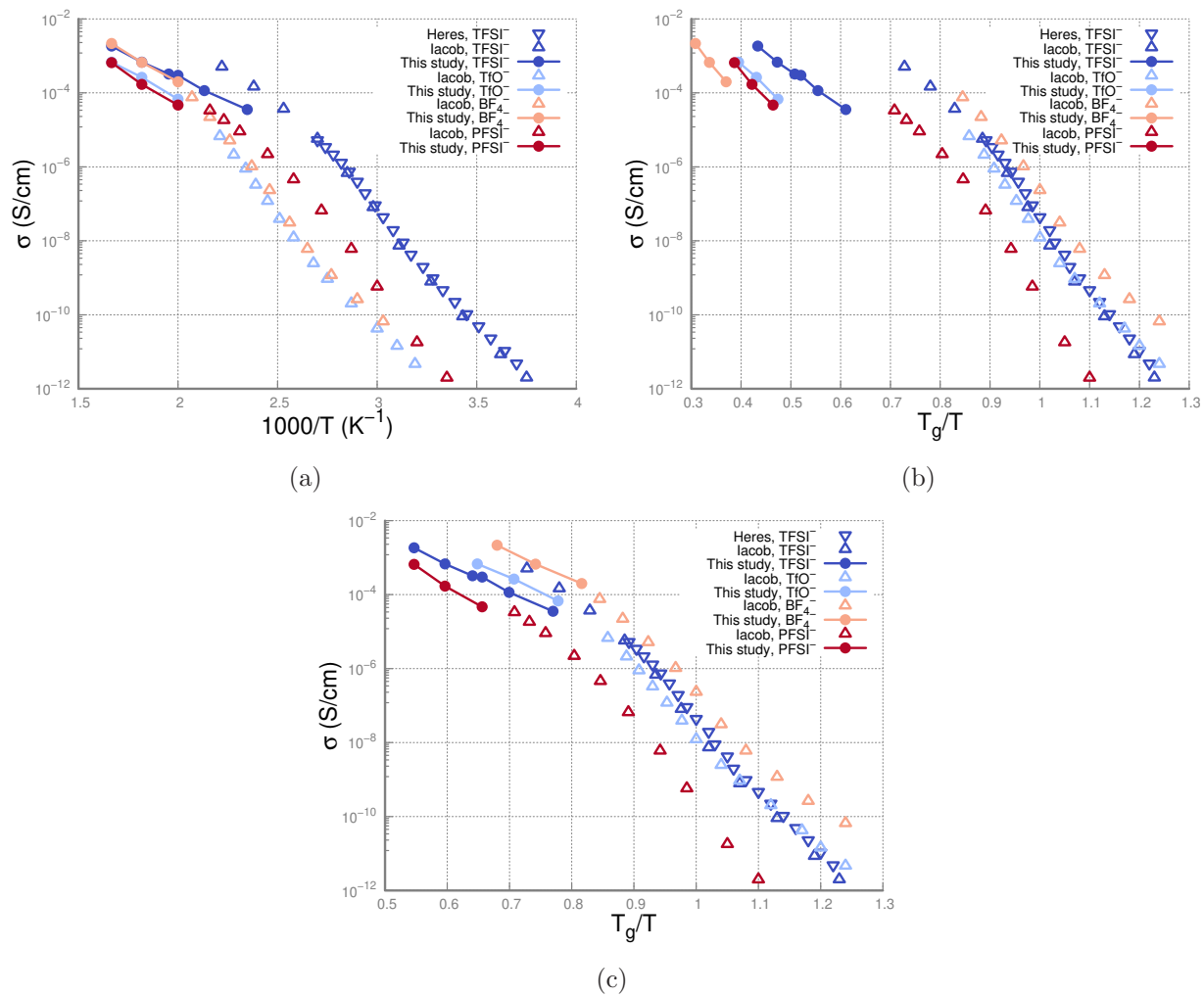


Figure S6: Experimental conductivities, reported by Heres 2019 (reference S44) and Iacob 2017 (reference S38). Nernst-Einstein conductivities of the same polyILs as reported in this study. Conductivity plotted against (a) $1000/T$, (b) T_g/T , and (c) adjusted T_g/T .

conductivity being lower in the simulation than in experiment, as pointed out in reference to the raw data in Figure S6(a).

It is unsatisfactory to compare simulation materials across temperatures normalized using a T_g based on experiment, just as it is foolish to expect that every system studied using atomistic simulation should exactly reproduce every static and dynamic property. The methodology used here to compute T_g is based on density, and many of the force field parameters used in this study were optimized to fit ionic liquid densities. While we cannot boast excellent fit to IL T_g either, we postulate that this may be the most critical source of error in computing T_g for the polymer systems: it results in a T_g far closer to the IL T_g than to that of the real polyIL. Based on the need to compare systems using intrinsic T_g , we settle for the imperfect T_g found from simulation, and any known (and unknown) outliers, including pBvIm⁺-BF₄⁻, must be acknowledged and considered when interpreting these results.

S3 Unreported results

S3.1 Diffusivity and Nernst-Einstein Conductivity

In this study, we used the Einstein relation to compute diffusivity from ensembles of mean-squared displacement (MSD):

$$D = \lim_{t \rightarrow \infty} \frac{1}{6t} \left\langle (\mathbf{r}(t) - \mathbf{r}(0))^2 \right\rangle. \quad (\text{S5})$$

We obtained the slope of the MSD by finding the line of best fit with the lowest standard error for a set of continuous points spanning at least 40% of production simulation time and beginning after at least 20% of the production run. We ceased trajectory collection after a minimum of 80 ns (120 ns for polyILs) of elapsed real time, or 80 (120) million timesteps of

NPT simulation. In many cases, longer production simulations were necessary for sufficient decay of $C(t)$ (discussed later). The power law fit of the MSD,

$$\langle (\mathbf{r}(t) - \mathbf{r}(0))^2 \rangle = C_0 \tau^\beta, \quad (\text{S6})$$

yields the parameter β , which can be used to characterize the linearity of the function.

Table S14: β linearity parameter for anions in all systems and temperatures

anion	IL_{300K}	IL_{350K}	IL_{400K}	IL_{450K}	$polyIL_{500K}$	$polyIL_{550K}$	$polyIL_{600K}$
AlCl_4^-	1.0001	0.99306	0.99522	1.0017	0.99213	0.99961	0.97382
BF_4^-	0.99083	0.99944	1.0012	0.99948	0.94208	0.9949	1.0099
Br^-	1.002	1.0023	1.008	0.98866	1.0083	1.0038	0.93964
Cl^-	0.84264	1.0032	1.0013	0.99114	0.9827	0.95703	0.99264
PfO^-	0.99112	1.0009	1.0099	1.0039	0.95254	0.92745	0.99193
PFSI^-	0.9977	0.99911	1.0018	0.99632	0.99227	0.95673	0.99454
TfO^-	0.99934	1.0051	0.99344	0.99445	0.98079	1.0033	0.98691
TFSI^-	0.99082	0.99036	0.99914	0.99711	0.97983	0.97015	0.99516

Table S14 shows the quality of the results reported in this work. All β fall within 20% of unity. Excluding $\text{BmIm}^+\text{-Cl}^-$ at 300 K, all linearity parameters fall within 10% of unity. Further excepting $\text{pBvIm}^+\text{-PfO}^-$ at 550 K, all values are within 5% of unity. Table S15

Table S15: β linearity parameter for cations in all systems and temperatures

anion	IL_{300K}	IL_{350K}	IL_{400K}	IL_{450K}
AlCl_4^-	1.0025	1.0077	0.99371	1.0091
BF_4^-	0.98842	0.9935	0.99377	0.99482
Br^-	0.97428	0.99276	1.0047	1.0027
Cl^-	1.0107	0.99394	0.99972	1.0042
PfO^-	1.0094	0.98953	0.99833	1.0035
PFSI^-	1.0029	0.99805	1.0076	1.001
TfO^-	1.0001	0.99097	0.99747	0.99289
TFSI^-	1.0027	0.97626	1.0083	1.0058

shows that β for the cation MSDs are even better behaved, all falling within 3% of unity. Excepting two cases ($\text{BF}_4^-_{300K}$ and Br^-_{300K}), the rest fall within 1% of unity. Figure S7 shows

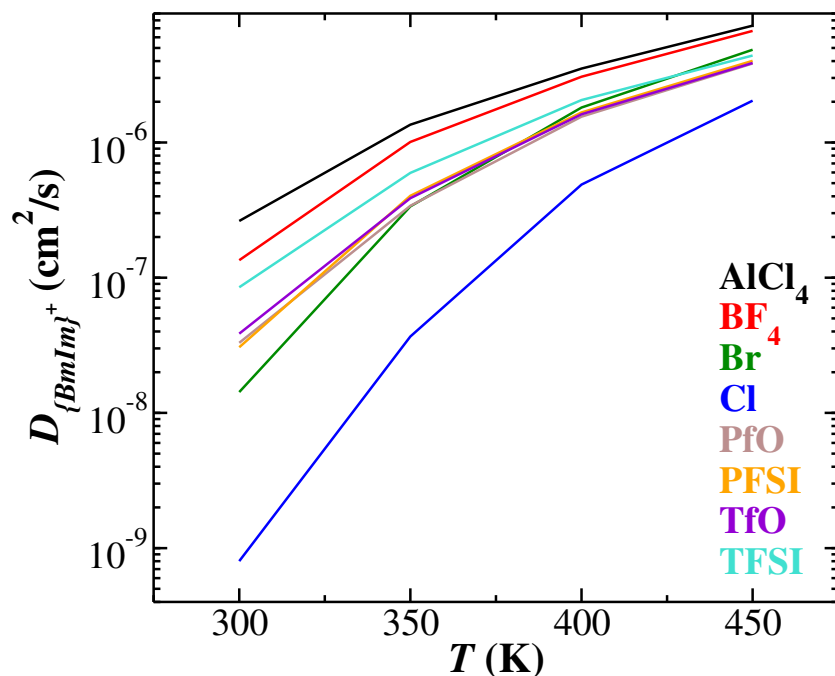


Figure S7: BmIm^+ diffusivity for all systems and temperatures

the diffusivities of the BmIm^+ cations for each system and temperature. Figures S8 and S9 show MSD curves for all mobile ions in IL and polyIL systems. There are two mobile ion types in the IL systems, represented by dotted (BmIm^+) and solid (anions) lines. Figure S10 summarizes anion diffusivities for all IL and polyIL systems and temperatures. A few salient features emerge from this figure. First, anions in ILs show a markedly steeper decline in the logarithm of diffusivity than their polyIL counterparts. Additionally, the negative concavity of the IL anion diffusivity curve suggests that probing lower temperatures would reveal increasingly steep declines for all species. For polyIL anions, the linearity in Figure S10 is striking, but no direct comparisons with ILs are possible due to the difficulty of accessing dynamical properties for these systems at low temperatures.

While diffusivity is effective for quantifying ion mobility, conductivity is a more important feature for designing materials for electrochemical devices. The Nerst-Einstein conductivity

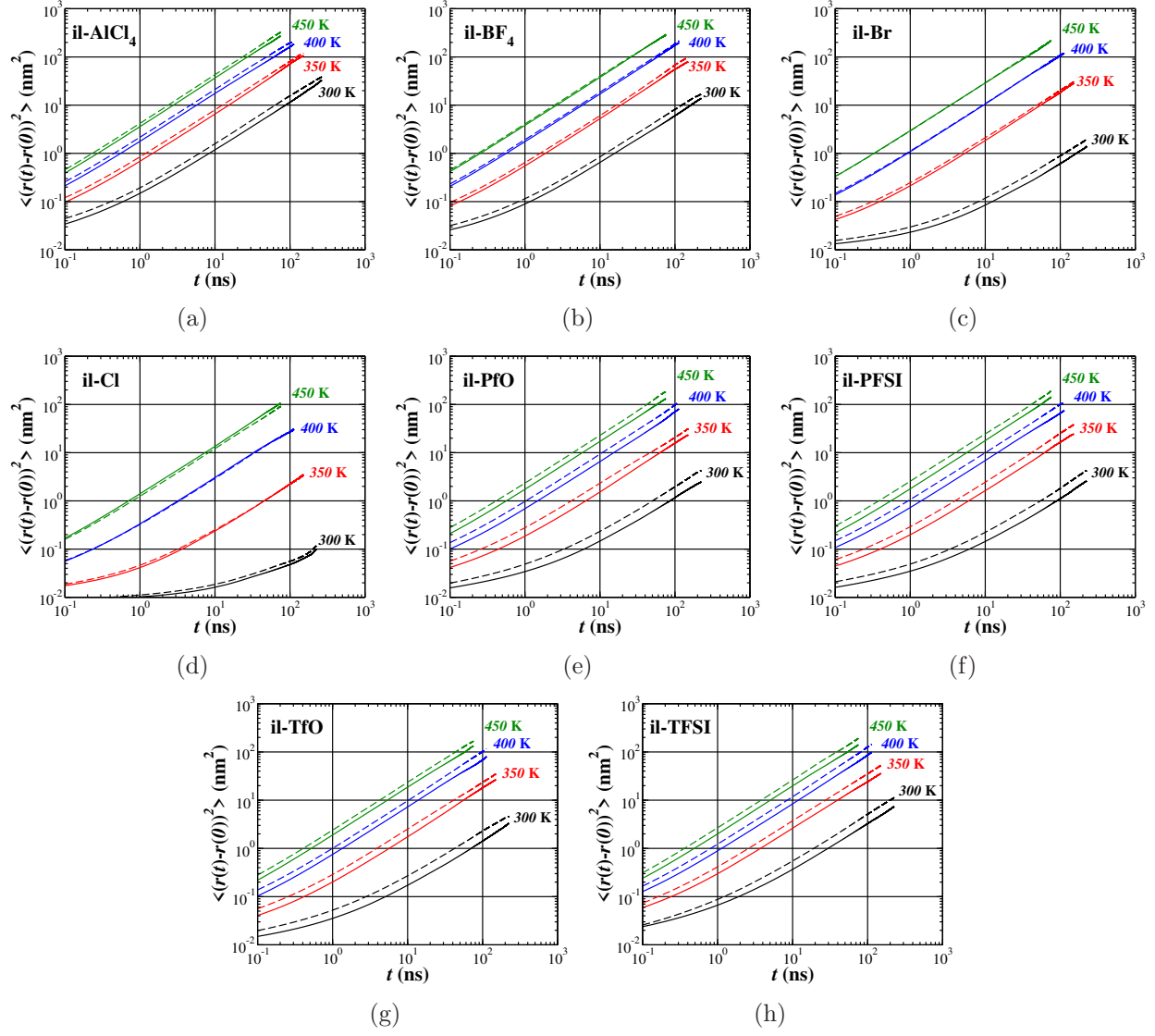


Figure S8: MSD for all ILs, anions, and temperatures.

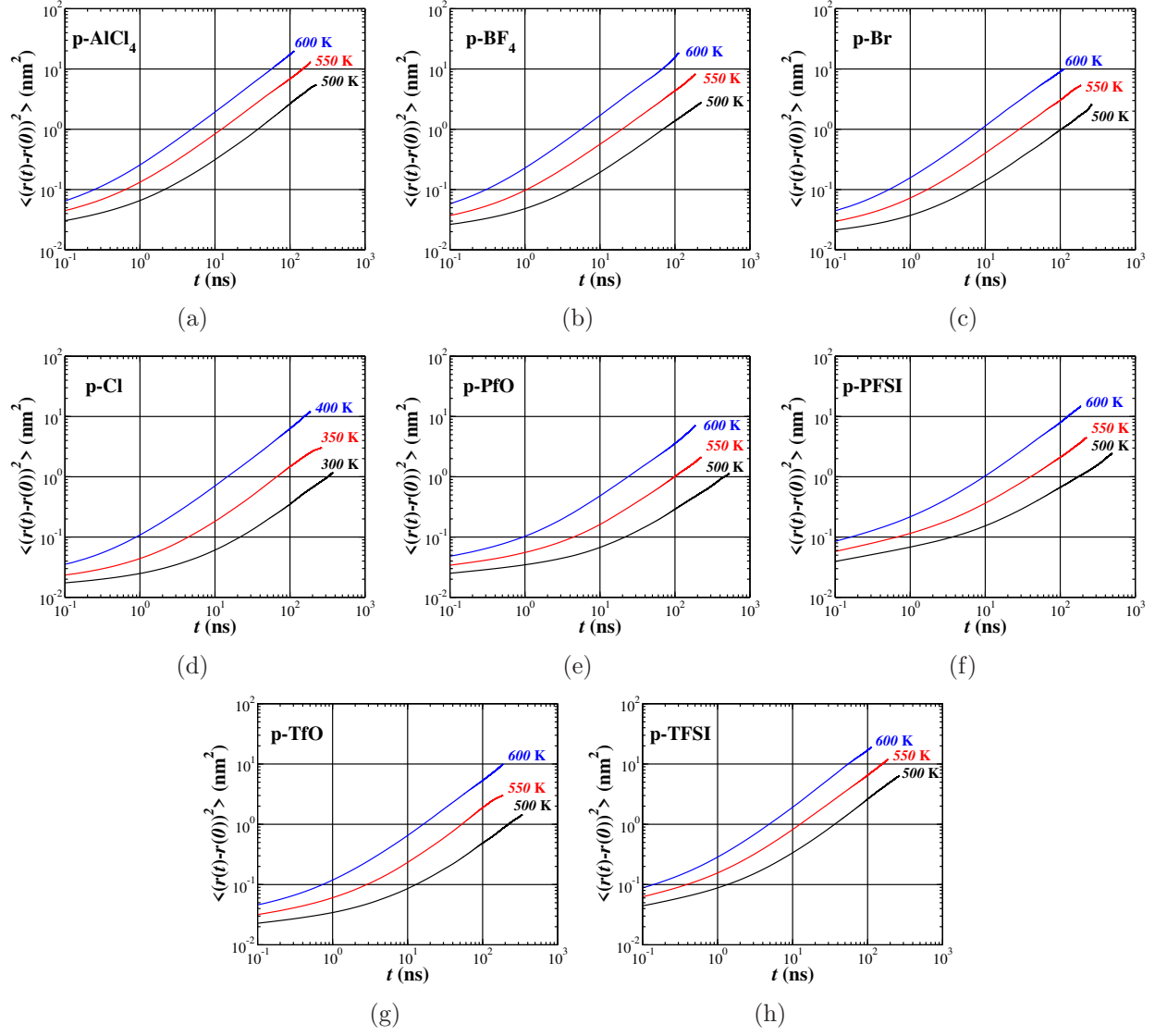


Figure S9: MSD for all polyILs, anions, and temperatures.

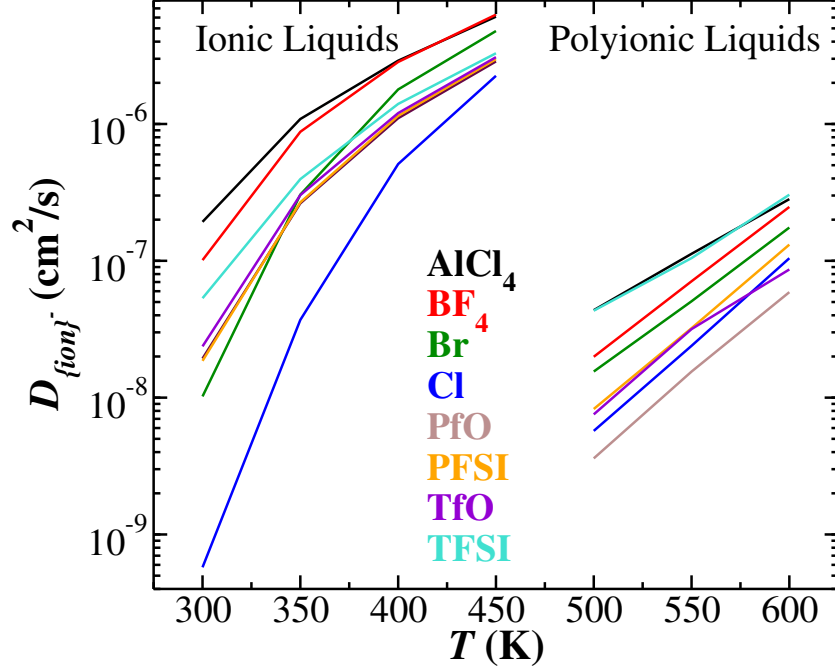


Figure S10: Anion diffusivity for all ILs and polyILs included in this study

(σ_{NE}), given by

$$\sigma_{NE} = \frac{N_{pair}}{Vk_B T} (q_+^2 D_+ + q_-^2 D_-) \quad (S7)$$

for a bicomponent ionic system, is sometimes used in computational studies due to the ease of computing diffusivity, as discussed above. Derived from such a form, Figure S11 unsurprisingly shows similar trends to those identified in diffusivity.

S3.2 dc Conductivity

Calculations of dc conductivity from simulations are fraught with uncertainties due to the accompanying statistical issues.^{S45} Hence, we did not report or discuss these results in the main article.

We calculated dc conductivity directly using the Einstein relation, a modified version of

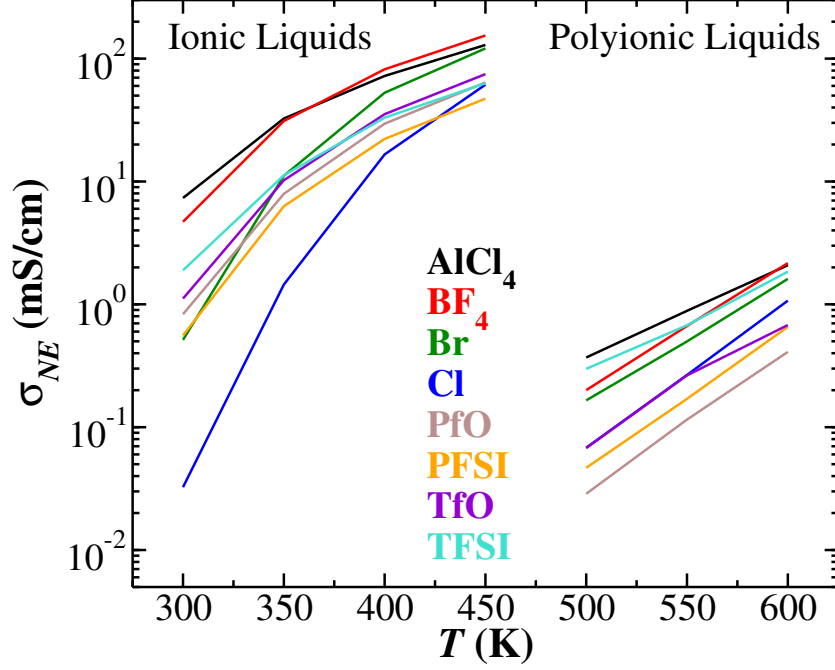


Figure S11: Nernst-Einstein conductivity plotted against temperature from IL and polyIL systems. ILs are shown at lower temperatures, with polyILs at higher temperatures.

the MSD ensemble that is shown in this equation:

$$\sigma_{dc} = \lim_{t \rightarrow \infty} \frac{e^2}{6tVk_BT} \sum_{ij}^N z_i z_j \left\langle [r_i(t) - r_i(0)] [r_j(t) - r_j(0)] \right\rangle. \quad (\text{S8})$$

We extracted the slope of the long-time average to obtain the dc conductivity. Due to significant fluctuations at large t , we were forced to discard time scales of greater than 50% of simulation times. In addition, to quantify the uncertainty inherent in our approach, we chose to represent the ultimate conductivity as the average of a series of linear fits on distinct data ranges from 0-50% of the simulation time. This average value, and its associated standard deviation, provided the reported results for σ_{dc} and the associated error bars. Figures S12 and S13 show the result of the Einstein relation of Equation S8 with all ion-ion (including self) interactions included (solid lines), plotted with the result when only considering self-correlations (dotted line), which would derive the Nernst-Einstein conductivity.

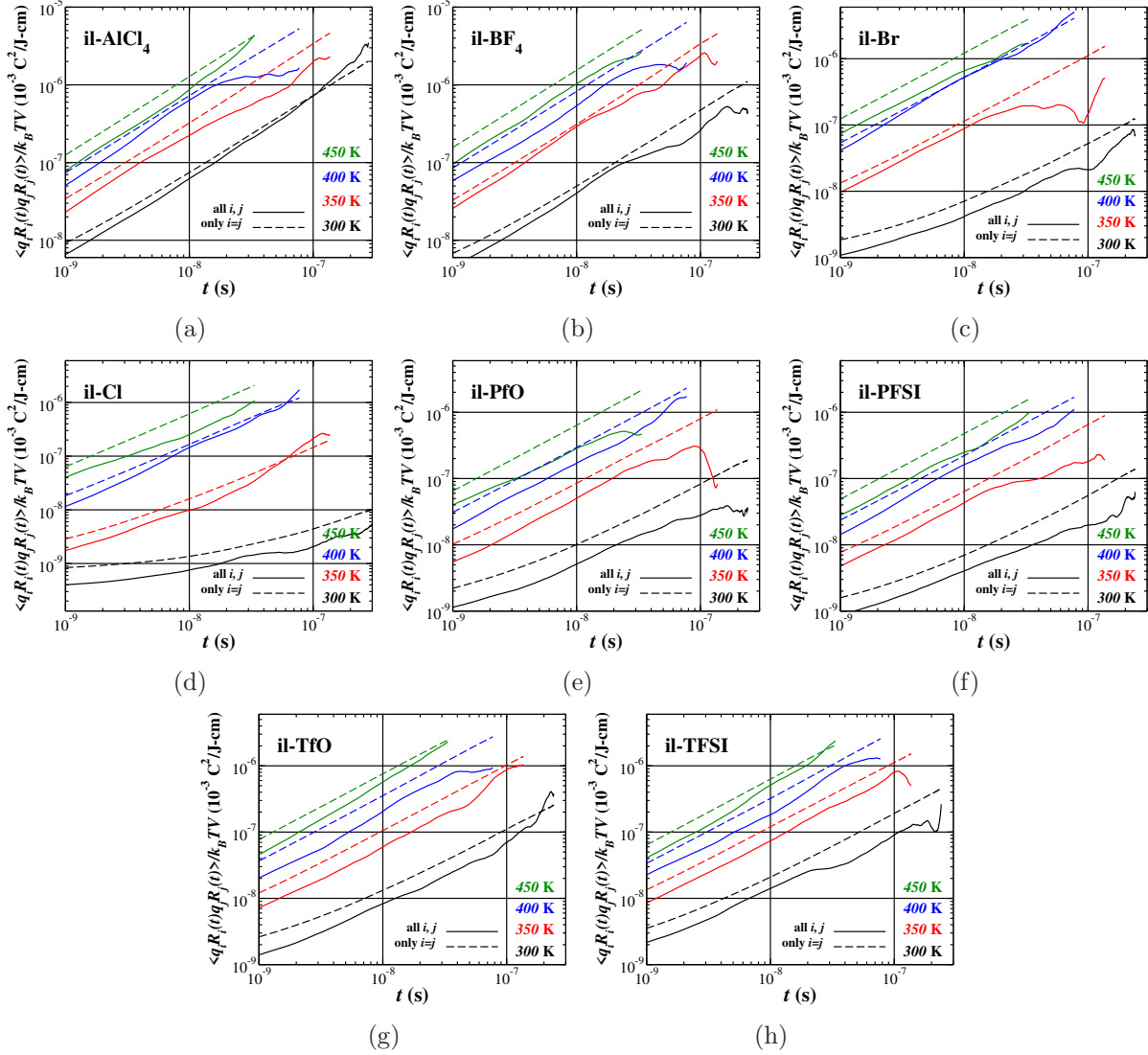


Figure S12: The Einstein relation result for all ILs, anions, and temperatures. Dotted lines represent results from just self-correlated motion (i.e. Nernst-Einstein), while solid lines include cross-correlation effects.

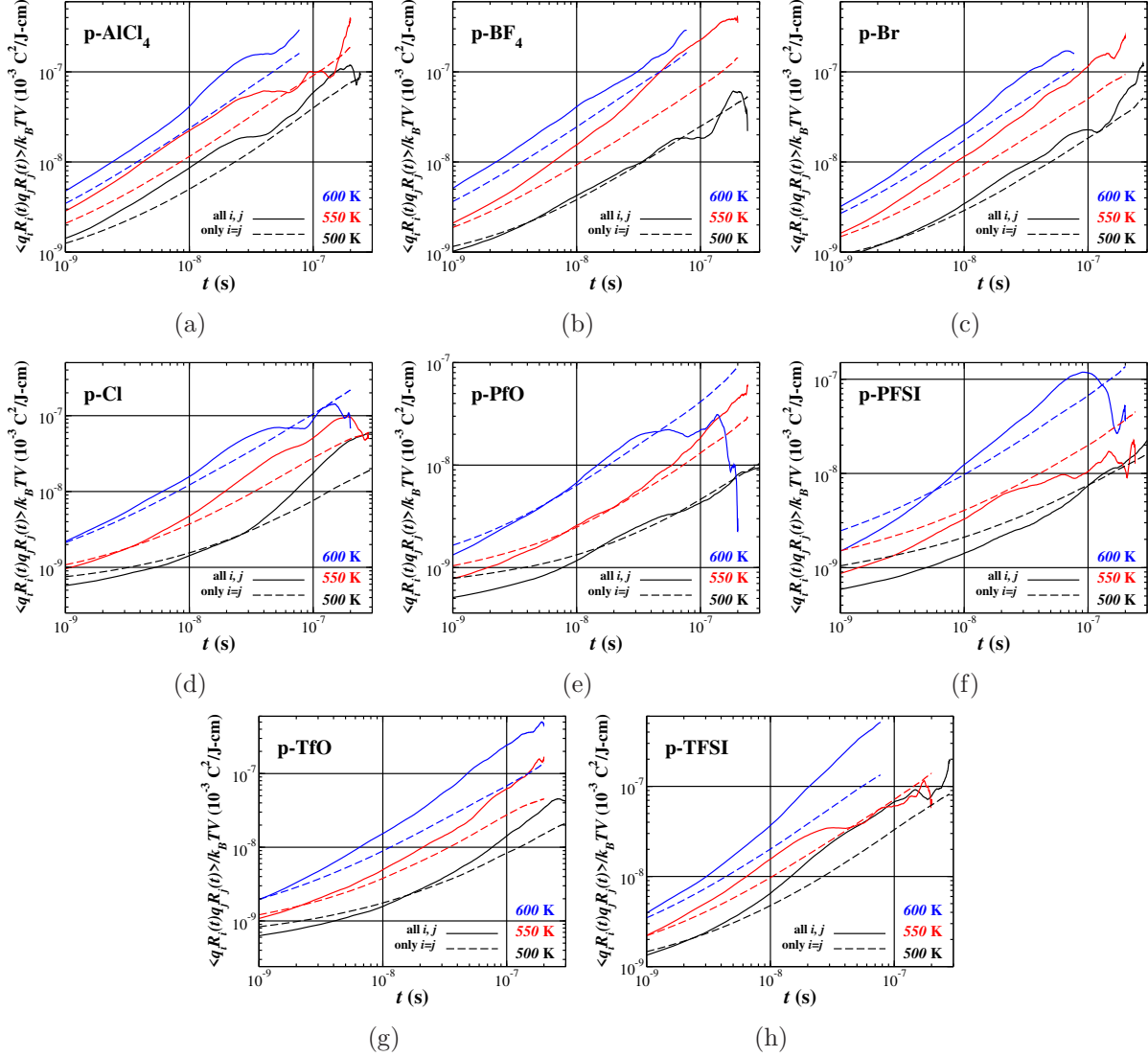


Figure S13: The Einstein relation result for all polyILs, anions, and temperatures. Dotted lines represent results from just self-correlated motion (i.e. Nernst-Einstein), while solid lines include cross-correlation effects.

Before leaving our discussion of conductivity, we must comment on the theoretical underpinning for choosing the Nernst-Einstein conductivity as our mobility representation. We extract anion diffusivity from the ensemble average mean-square displacement (MSD) over time and as an average of the contribution from all anions. The implicit assumption within this analysis is that all anions are mobile. Thus, from equations S5 and S7, one could rationalize the following transformation to reveal the theoretical basis for the Nernst-Einstein conductivity in the systems under study.

$$\sigma_{NE} = \frac{N_{pair}}{Vk_B T} \left(q_+^2 \left(\lim_{t \rightarrow \infty} \frac{\langle MSD_- \rangle_t}{6N_- t} \right) \right) \quad (S9)$$

Since there is one anion per pair, $N_{pair} = N_-$. We also know that $D_+ \ll D_-$ for the systems and temperatures under consideration. This results in an equation that is similar in form to equation S8

$$\sigma = \lim_{t \rightarrow \infty} \frac{e^2}{6tVk_B T} \sum_i^{N_-} z_i^2 \langle MSD_i \rangle_t \quad (S10)$$

Equations S9 and S10 are functionally equivalent, proving that the Nernst-Einstein assumption is justified, and mobile ion density is correct.

S3.3 Relaxation timescales

In past work, ion-association dynamics have been a key thrust of our efforts in polyIL simulations. The intermittent ion-association autocorrelation function $C(t)$ is defined as follows:

$$C(t) = \frac{\langle h(t_0)h(t_0 + t) \rangle}{\langle h \rangle}, \quad (S11)$$

where $h(t)$ takes a value of one if a pair of ions is associated and zero otherwise.^{S9–S11} In essence, $C(t)$ represents the probability of two ions being associated at time t given that they were associated at time $t = 0$. We smooth the result by fitting a stretched exponential

of the form

$$C(t) = a_0 \exp \left(- \left(\frac{t}{a_1} \right)^{a_2} \right), \quad (\text{S12})$$

with the timescale for relaxation taking the form

$$\tau_C = a_0 a_1 \Gamma \left(1 + \frac{1}{a_2} \right), \quad (\text{S13})$$

which is most easily understood as the probability that two ions are “associated” at time t

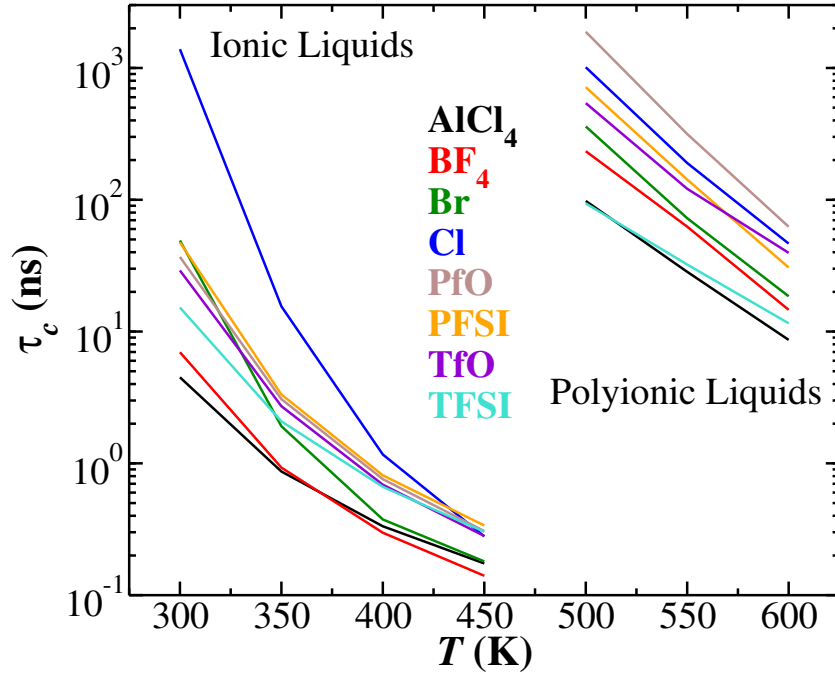


Figure S14: Ion-association structural relaxation times for all systems and temperatures.

if they were associated at time $t = 0$. Note that all this information is conveyed in the same detail within the main text. This function decays with a characteristic timescale τ_C , which we proved in prior works was well-correlated with the structural relaxation time computed from the decay of the maximum of the first peak in the self-intermediate scattering function.^{S9} To distinguish between the two values, we assign τ_C the moniker “ion-association structural relaxation time,” with the implicit connection to the structural relaxation time assumed.

Additionally, we computed the continuous ion-association autocorrelation function, $S(t)$, whose characteristic timescale is the average lifetime of ion-association “pairs.” This function is defined by

$$S(t) = \frac{\langle h(t_0)H(t_0 + t) \rangle}{\langle h \rangle}, \quad (\text{S14})$$

where the new association variable $H(t)$ is described by the following:

$$H(\tau) = \begin{cases} 1, & (h(t) = 1) \forall (t_0 \leq t < t_0 + \tau) \\ 0, & \text{otherwise.} \end{cases} \quad (\text{S15})$$

As with τ_C , we fit $S(t)$ to a stretched exponential form

$$S(t) = a_0 \exp \left(- \left(\frac{t}{a_1} \right)^{a_2} \right), \quad (\text{S16})$$

and the characteristic timescale was evaluated as

$$\tau_S = a_0 a_1 \Gamma \left(1 + \frac{1}{a_2} \right). \quad (\text{S17})$$

Figures S15 and S16 show the autocorrelation functions $C(t)$ and $S(t)$ for all systems and temperatures. $C(t)$ is represented by solid lines and $S(t)$ by dotted lines, and both are displayed for each counterion for polyILs and ILs. The average lifetime of ion-association pairs is plotted on a logarithm scale versus temperature for all systems in Figure S17. While τ_C for the halide ions showed much higher relaxation times compared with the other ions, they show low values for τ_S . We are not able to explain the result for Br^- at 450 K, and suggest ignoring this outlier for the purpose of evaluating trends.

How does the τ_C behave when normalized with respect to polymer dynamics using T/T_g ? Figure S18 reveals IL curves with positive concavity, showing τ_C increases more steeply as the

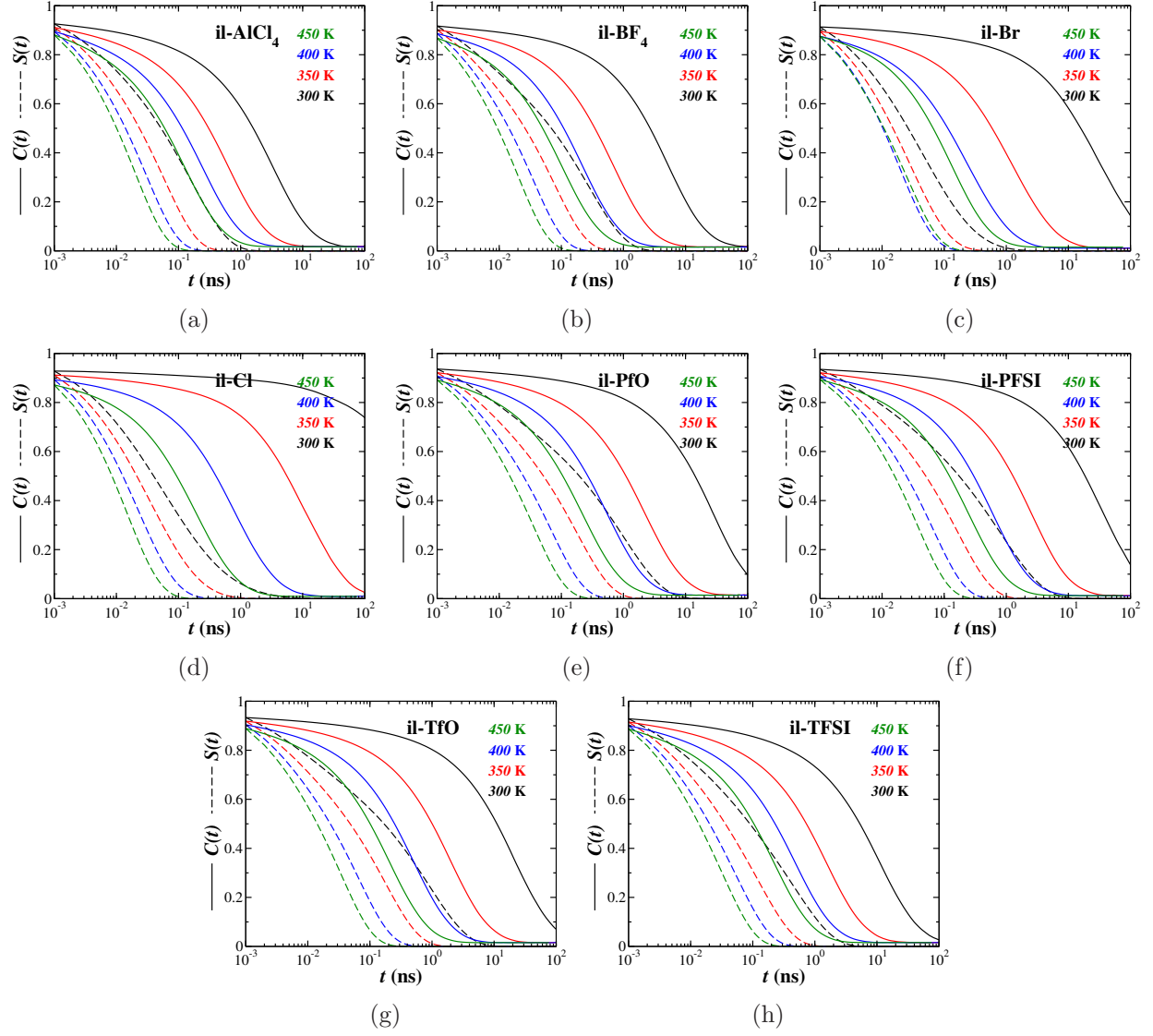


Figure S15: Intermittent ($C(t)$) and continuous ($S(t)$) ion-association autocorrelation functions for all ILs and temperatures. $C(t)$ shown by solid lines and $S(t)$ by dotted lines.

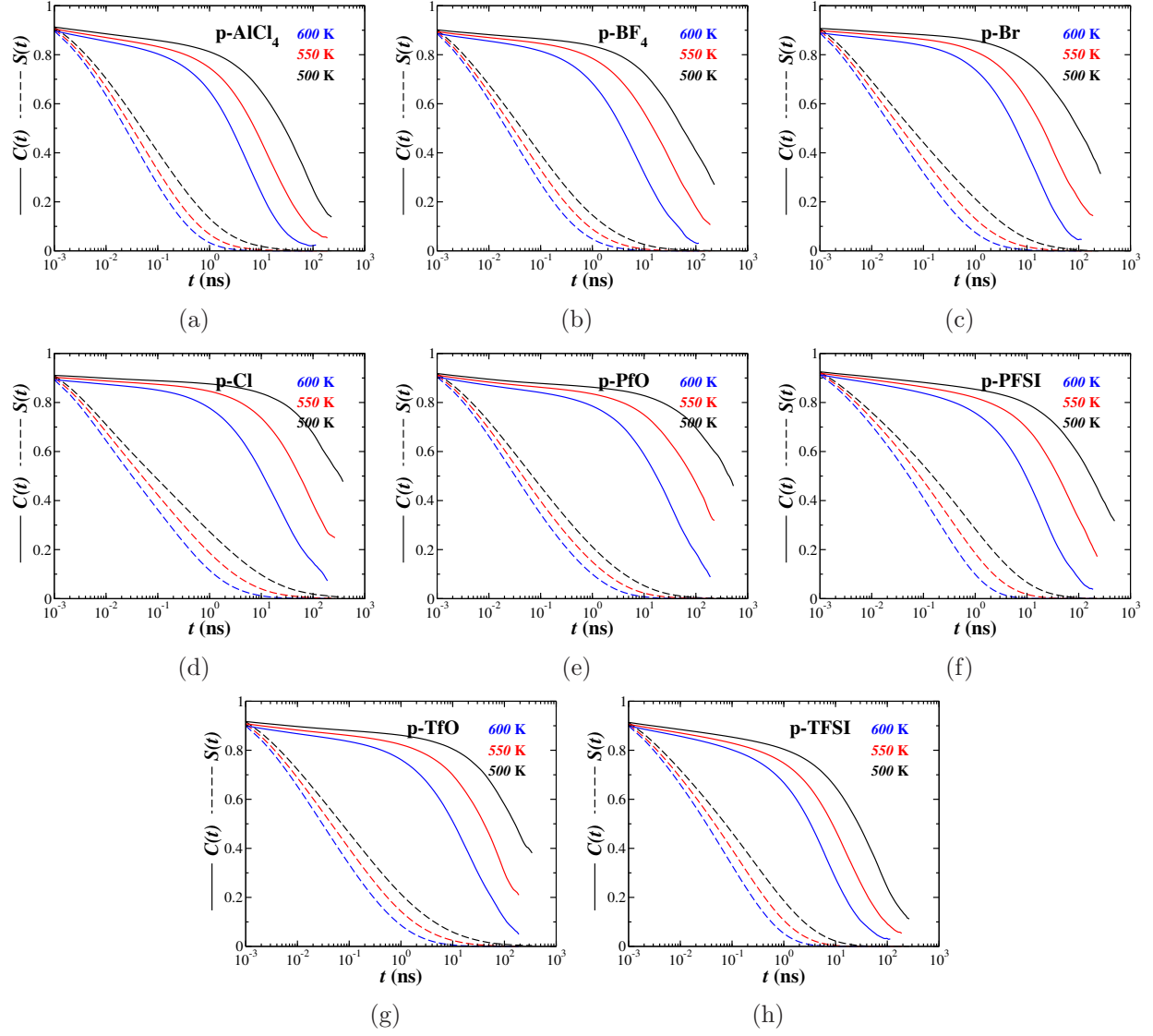


Figure S16: Intermittent ($C(t)$) and continuous ($S(t)$) ion-association autocorrelation functions for all polyILs and temperatures. $C(t)$ shown by solid lines and $S(t)$ by dotted lines.

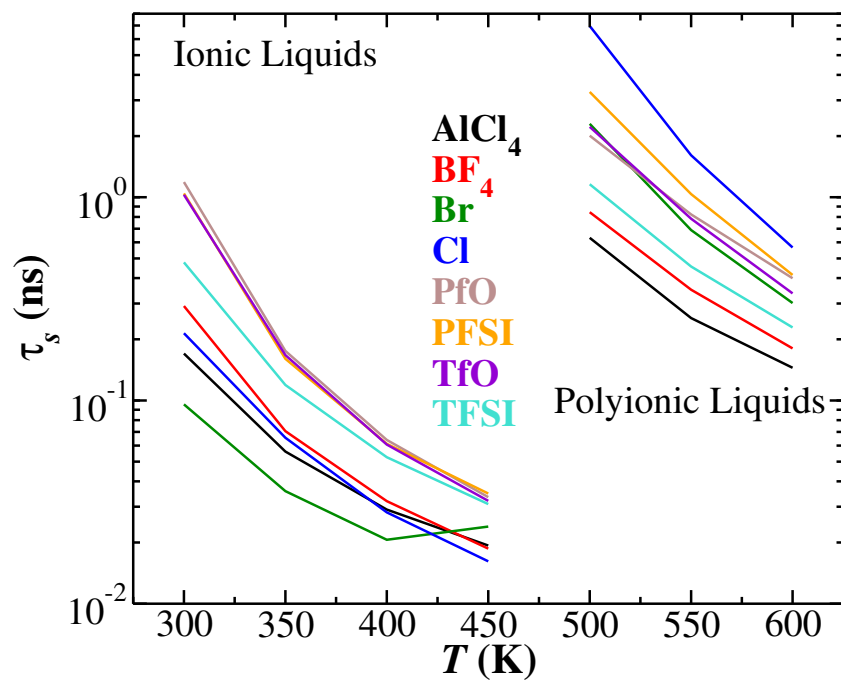


Figure S17: Average lifetime of ion pairs versus temperature for all systems.

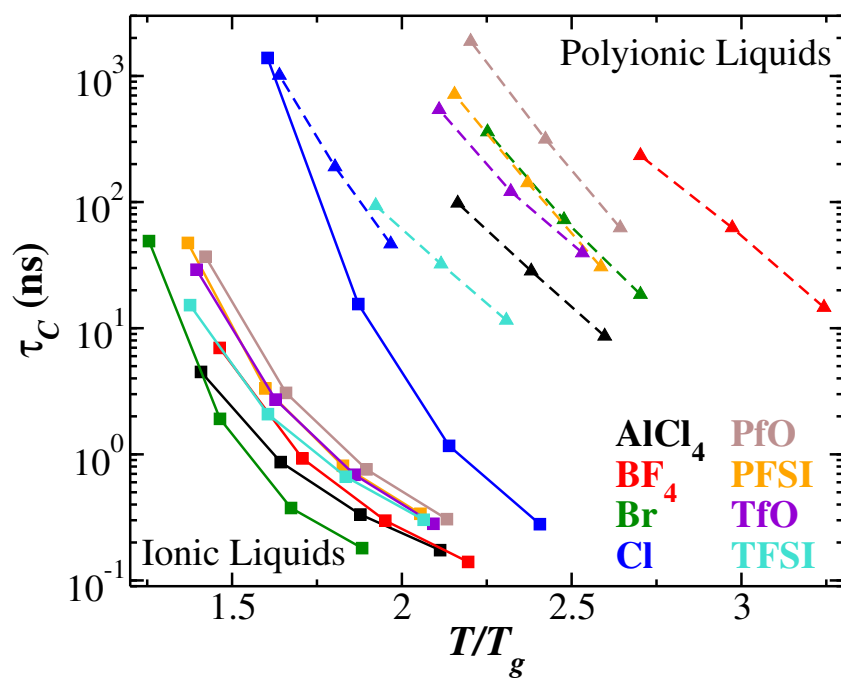


Figure S18: The ion-association structural relaxation time compared against T_g/T , for ILs (solid lines with square symbols) and polyILs (dashed lines with upward triangle symbols).

temperature approaches T_g . The pBvIm⁺-Cl⁻ and BmIm⁺-Cl⁻ lines appear poised to cross, whereas these curves crossed within our temperature range for diffusivity and conductivity. This could be indicative of decoupling between conductivity and polymer dynamics in the Cl⁻ polyIL. Comparing polymer results across T/T_g for these relaxation times, we note the following order of decoupling in ion and polymer dynamics: BF₄⁻ < PfO⁻ < Br⁻ \approx PFSI⁻ < TfO⁻ < AlCl₄⁻ < TFSI⁻ < Cl⁻. This is consistent with the results obtained in diffusivity.

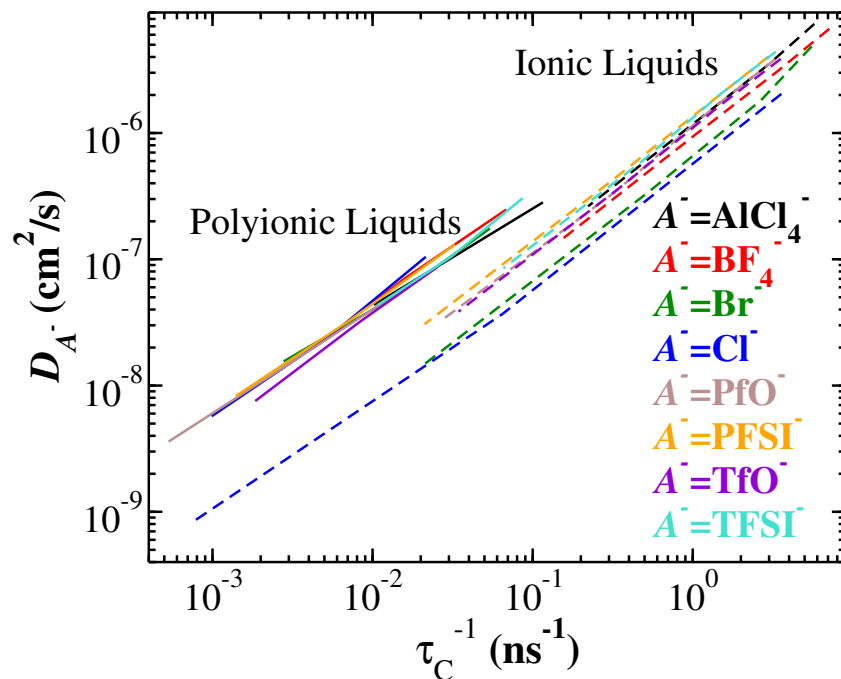


Figure S19: Diffusivity plotted against inverse ion-association relaxation time.

Figure S19 demonstrates that the polyIL diffusivity versus τ_C curves overlap, supporting this interpretation.

S3.4 Local structural coordination

To characterize the structural features of our system, we calculated the radial distribution functions $g(r)$ between like and oppositely charged ions. The function $g(r)$ is computed

using the following formalism:

$$g(r) = \frac{\rho(r)}{\rho_0}, \quad (\text{S18})$$

where $\rho(r)$ is the average density of particles calculated within discrete 0.04 Å thick spherical shells, and ρ_0 is the expected density of uniformly distributed particles. We note two observations in each curve in Figure S20(e): 1) the value of $g(r)$ at the maximum of the first peak and 2) the value of the radius at which $g(r) = 1$. The latter is deemed the “cutoff radius” for the purpose of evaluating ionic coordination behavior and ion-association states for dynamic ion pair relaxation analysis, as was described in Section S2.1. Spherically symmetric ions show an increasing cutoff distance roughly consistent with ion size based on experimental ion volumes (see SI section S2.2 for details): $\text{Cl}^- < \text{Br}^- < \text{BF}_4^- < \text{AlCl}_4^-$. $\text{pBvIm}^+\text{-Cl}^-$ clearly shows two peaks that can be deconvoluted around 4 Å and a third association peak inside the cutoff radius. It appears as if $\text{pBvIm}^+\text{-Br}^-$ also has three associative peaks within the computed cutoff radius. The fluoro-alkyl sulfates TfO^- (violet) and PfO^- (brown) are comparable in maximum-first-peak radius and cutoff distance, but PfO^- shows a higher peak, implying stronger binding to the polymer ions. The bis-(fluoroalkylsulfonyl)imides also show similar cutoff distances, as well as significant spreading of the first peak. Once again, the larger ion (PFSI^-) has a smaller maximum peak radius and a higher maximum in the first peak implying stronger binding to the cationic polymers.

In the main article, we discussed the salient features of the full $g(r)$, particularly for AlCl_4^- . The full deconvoluted $g(r)$ (broken down by nearest-neighbor ion) for all species are shown in Figure S21. We will now elaborate on a few features of the three best performers in the main article. $\text{pBvIm}^+\text{-Br}^-$ (Figure S21(c)) shows features similar to those identified in Cl^- (Figure S21(c)), suggesting that these two ions share similar local coordination features, including bulky ionic aggregates whose organization is influenced by the connectivity of polymerized monomers. The split between the first and second coordination shells is visible at a

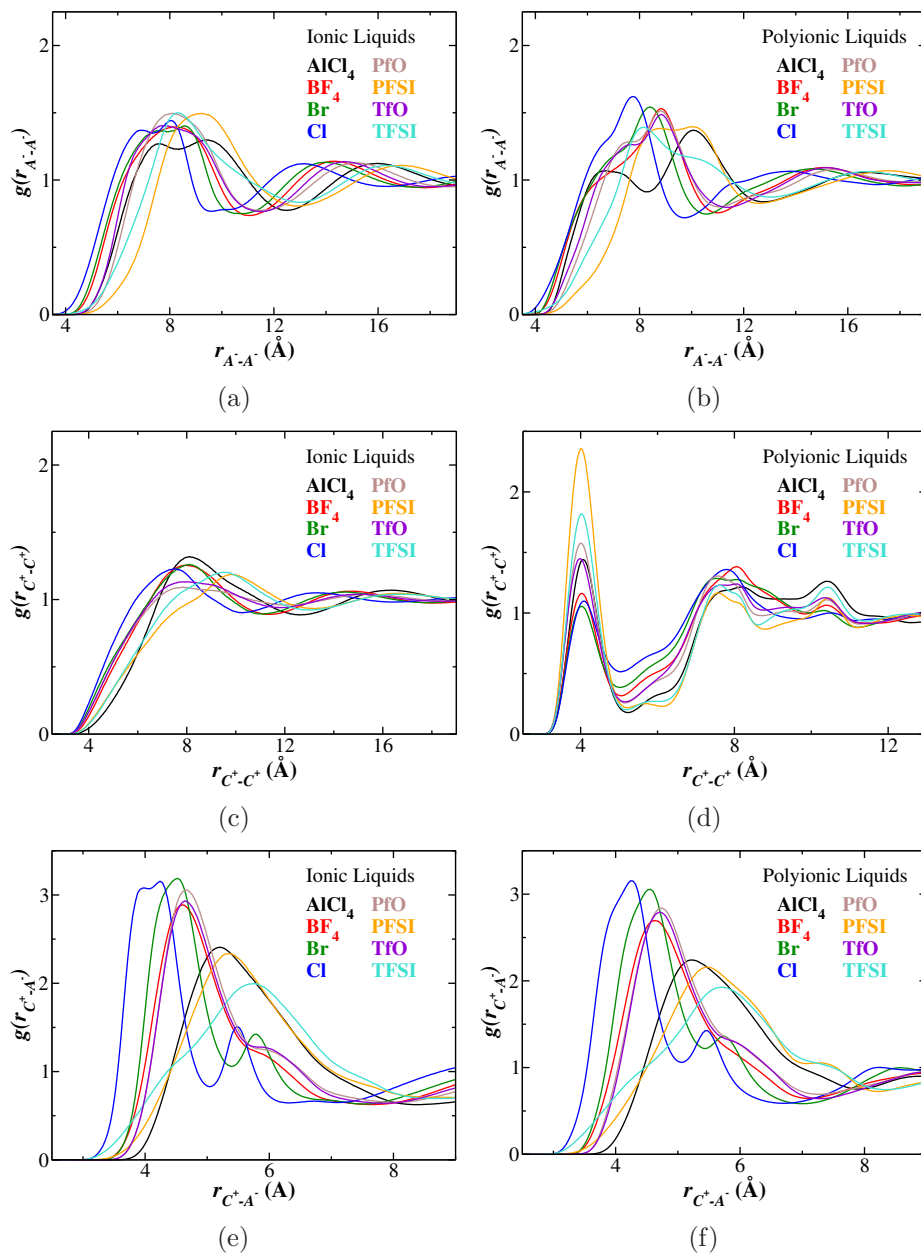


Figure S20: Radial distribution function for all ILs (a,c,e 450 K) and polyILs (b,d,f 500 K). a) and b) correspond to anion-anion coordination, c) and d) to cation-cation coordination, and e) and f) to cation-anion coordination. Part f is a reproduction of Figure 4(a) from the main article

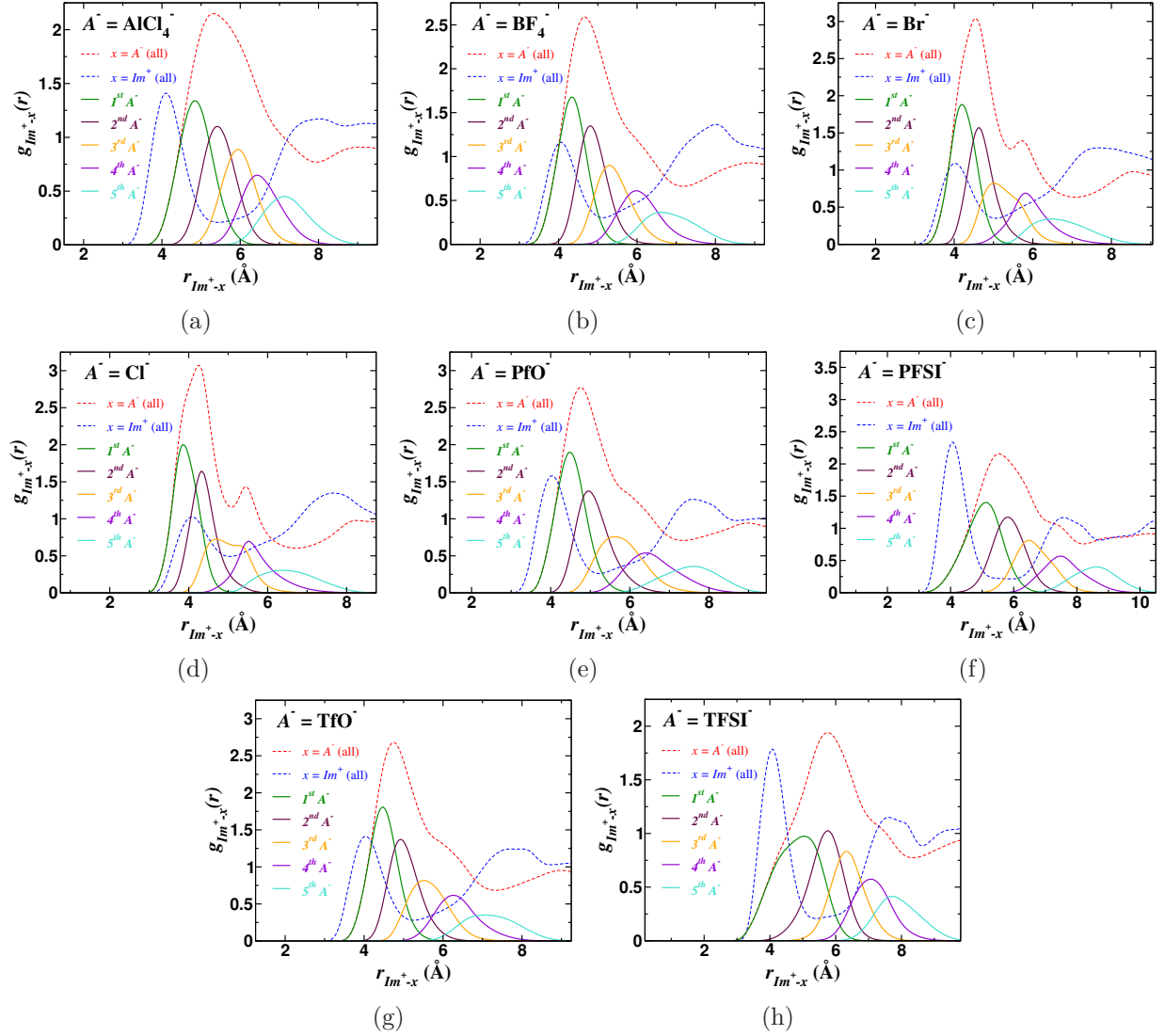


Figure S21: Deconvoluted radial distribution function for all polyILs at 600K: a) AlCl_4^- , b) BF_4^- , c) Br^- , d) Cl^- , e) PFO^- , f) PFSI^- , g) TfO^- , and h) TFSI^- . Dotted lines correspond to full $g(r)$ for cations-anions (red) and cations-cations (blue). Solid lines correspond to nearest-neighbor ions as described in the legend.

slightly higher distance than found in $\text{pBvIm}^+\text{-Cl}^-$. Considering Figure S21(b) for $\text{pBvIm}^+\text{-BF}_4^-$ with these two systems, we can identify similarity in the shape of a hypothetical curve traced through the maxima of each nearest-neighbor peak. For $\text{pBvIm}^+\text{-AlCl}_4^-$, that curve looks roughly linear. On the other hand, each of the other spherical systems show distinct weighting to lower distance. This is driven by closer association and subsequent exclusion of ions outside of the first coordination shells. This same feature is evident in the sulfate ions, whereas the sulfonylimides show features consistent with the $\text{pBvIm}^+\text{-AlCl}_4^-$ curve.

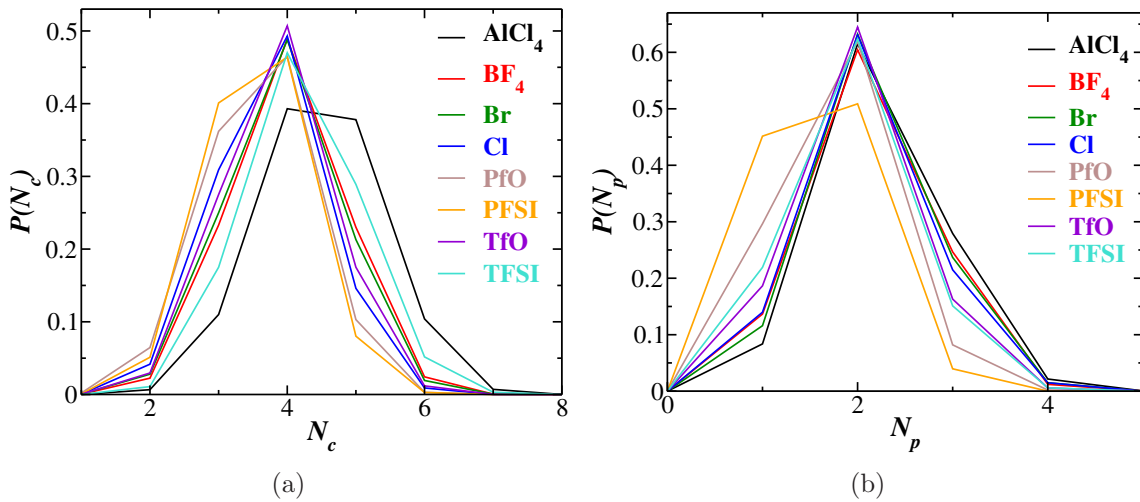


Figure S22: Population statistics for number of a) coordinating ions (N_c) and b) polymers (N_p) for polyILs at 600 K. Figure a) is replication of Figure 4(b) from the main paper for clarity of discussion.

Figure S22 shows the population statistics of the polyIL systems for number of coordinating ions and polymers. Figure S22(a) is a reproduction of Figure 4(b) of the main paper, which displays the population statistics of ionic coordination. Beginning with the spherically symmetric ions, the coordination number increases monotonically with size: $\text{Cl}^- < \text{Br}^- < \text{BF}_4^- < \text{AlCl}_4^-$. An inverse relationship thus emerges between the cutoff distance and the strength of association, as characterized by the maximum peak quantity for $g(r)$. This reveals the following physical interpretation: small ions are associated more regularly (more lattice-like) due to the lesser volume exclusion, while large ions are smeared across

a larger volume, and are thus present in greater numbers within a given cutoff radius. In fact, pBvIm⁺-AlCl₄⁻ is starkly different than most of the materials in this study, showing a broader population distribution with an average and maximum value significantly removed from the closest ion, TFSI⁻. In the sulfates and sulfonylimides, the larger ionic species has a lower coordination number, which is opposite to the spherically symmetric ions. We rationalize this result with the following addendum to the original physical interpretation. For ions deviating from spherical geometry, all local structural distributions are smeared by the irregularity of the side group fluorocarbons.

For the polymer coordination number observable in Figure S22(b), we see that all ions have a maximum at $N_p = 2$. The largest linear ion pBvIm⁺-PFSI⁻ is the most smeared and has the lowest average polymer coordination number, and caps a trend that suggests that larger linear ions are associated with fewer polymers. Conversely, the spherical ions appear to associate with a greater number of polymers as the ion increases in size, with pBvIm⁺-AlCl₄⁻ having the largest average polymer coordination number. It is unclear why the larger spherical ions would promote greater polymer-polymer interactions, and what influence this might have on the underlying transport mechanism. There is no evidence to suggest that polymer-to-polymer hopping events are more effective than intra-polymer ones, although more analysis is included later in this package.

What explains the high extent of decoupling for pBvIm⁺-AlCl₄⁻ and -TFSI⁻, two large, geometrically diverse ions? Recall that we identified the unique behavior of AlCl₄⁻ in the $g(r)$ from Figure 4(a) of the main article, showing a much weaker extent of coordination with the cations relative to the other spherical anions. We also pointed out in Figure 4(b) of the main paper that AlCl₄⁻ exhibits a much broader distribution and higher ionic coordination number, supporting the delocalization seen in the $g(r)$ plot. Figure S22(a) makes it clear that TFSI⁻ behaves similarly to AlCl₄⁻, with a distribution of ionic coordination numbers shifted higher than other ions. For the sake of completeness, we now consider Fig-

ure S22(b). It was previously postulated that PF_6^- diffuses by a mechanism involving, on average, four interacting cations and two interacting polymers.^{S9} Herein, we can see potentially two regimes emerging. First, as in PF_6^- -polyILs, spherically symmetric ions smoothly shift to higher ionic and polymer coordination numbers with increasing size. AlCl_4^- seems to buck the decoupling trend due to a strong jump in ionic coordination number. For the linear ions, with specific chemical groups, larger ions have lower ionic and polymer coordination numbers. The deviation from TFSI^- to PFSI^- within ionic coordination number is much greater than that from TfO^- to PfO^- . This could serve as a clue for why TFSI^- performs so well in decoupling. Regardless, it appears that the polymer coordination number does not provide the right context for evaluating decoupling phenomena. This is apparent by the locations of the top three performing ions, Cl^- , TFSI^- , and AlCl_4^- within the series (no correlation to the decoupling series). From the results developed in the deconvoluted $g(r)$ from Figures S21(a) and S21(h), we can surmise that the extra ionic coordination is fueled by gaps forming within the polymer matrix. Such gaps could be sufficiently large or appropriately spaced to facilitate movement in the absence of polymer rearrangement, driving the increased decoupling in AlCl_4^- and TFSI^- .

S3.5 Ion hopping signatures

In a past study, we presented results which supported ion hopping mechanism underlying the mobility of ions in polyILs.^{S11} We refer the interested reader to the SI for that article for a complete procedure and list of definitions for the various hopping frequencies. In short, we identify two types of ion hopping events, intra- and inter-molecular, which occur when ion-association pairs are formed or broken. Figure S23 shows the fraction of intra- and inter-molecular hopping events that happen as a distribution of the number of coordinated ions in the associated state. pBvIm^+ - PFSI^- and $-\text{PfO}^-$ both tend to be less coordinated during intra-molecular hopping events, and $-\text{Cl}^-$ to a lesser extent. AlCl_4^- is the most highly

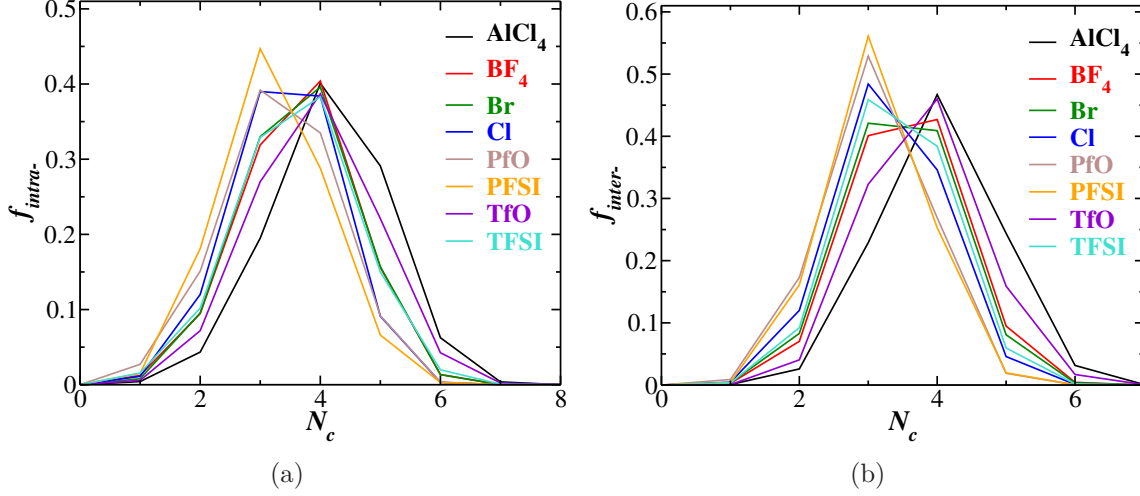


Figure S23: Probability distributions of coordination number (N_c) in the associated state for a) intra-molecular hopping events and b) inter-molecular hopping events.

coordinated ion is both hopping types, which is consistent with its distribution in the full coordination space, as shown in Figure 4(b) in the main paper. Generally, the ions studied here shift to lower coordination numbers to facilitate inter-molecular hopping. No discernable pattern can be identified in this data to assist in developing conclusions related to decoupling phenomena.

Figure S24(a) shows the frequency of hopping events for all ions at 600 K, ordered from left to right by increasing degree of decoupling, as defined in the main article. The open symbols represent the frequency of intra-molecular hopping events, the solid-filled symbols show the frequency of inter-molecular events, and the pattern-filled symbols display the sum of these two contributions (the total frequency). We see that there is no distinguishable pattern in this data. However, we note the uncertainty in this result, since the hopping frequency trend may manifest at the same T_g/T . However, this speculation is mitigated by the findings in Figure S24(b). Here, the frequency results for Cl^- and TFSI^- are extrapolated in all three hopping types using a simple linear regression to align with the T_g/T values from the other ions: 1) 600 K: AlCl_4^- , Br^- , TfO^- , PFSI^- , and PFO^- ; 2) 500 K: Br^- ; 3) other:

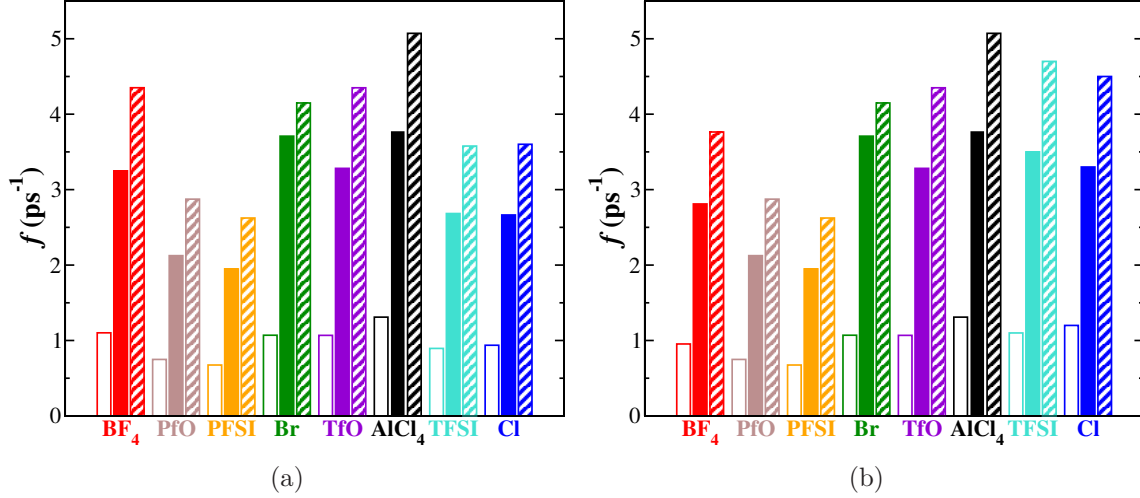


Figure S24: Open symbols are intra-molecular hopping frequency, solid-filled symbols are inter-molecular hopping frequency, and pattern-filled symbols are total hopping frequency. a) All three measures across ions (ordered by extent of decoupling from conductivity analysis) at 600 K. b) The same analysis as part a, plotted for ions (overlapping and extrapolated) at the same T_g/T .

TFSI⁻ (680 K), Cl⁻ (800 K). We are once again frustrated by results that are inconsistent with the decoupling identified in conductivity. Nevertheless, one very interesting conclusion is evident from these results: inter-molecular hopping constitutes the majority of hopping events observed in these systems.

To expand this result, we now dive deeper into a total hopping framework. Figure S25(a) plots the T_g -normalized ion hopping frequency (f_t), a quantity which has been defined and discussed in detail in Section S3.3 and previous works.^{S10,S11} The characteristic “cutoff” distance over which a hopping event occurs, differing for each ionic species, was evaluated to be the distance r at which $g(r) = 1$ following the first peak. It is clear that ion hopping frequency is not the only contribution to conductivity decoupling, since Figures 2 and S25(a) are not compatible.

This result seems inconsistent, since decoupling conductivity from segmental dynamics likely results from the replacement of polymer-coordinated motion with ion hopping. Consider, though, that ion hopping is a reversible process in which association states can be

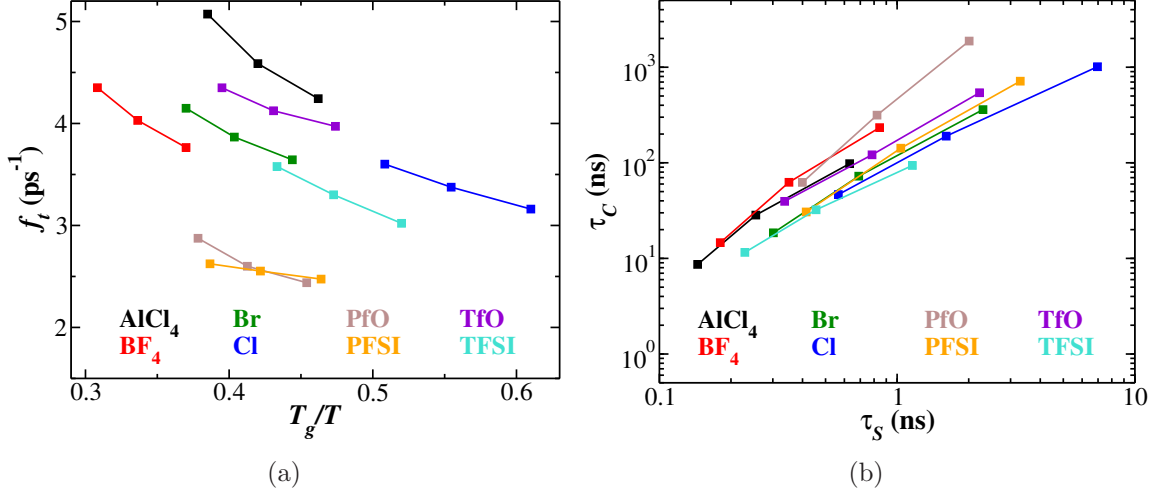


Figure S25: a) Comparison of the frequency of hopping events (f_t) at respective T_g/T s for all materials in this study. b) Plot of the ion-association structural relaxation time (τ_C) with the average ion-pair lifetime (τ_S) to illustrate the comparative reversibility of ion hopping events for each material.

separated by low activation barriers. More importantly, the reversibility of hopping events may vary considerably for anions of different shapes and sizes. In Figure S25(b), the abscissa is average lifetime of ion pairs (τ_S), the ordinate is ion-association structural relaxation time (τ_C), and the ratio of these timescales serves as a benchmark for hopping reversibility. We have exhaustively defined and discussed these values in Section S3.3 and previous publications.^{S9–S11} The ratio τ_C/τ_S represents the number of “conductivity-neutral” hopping events per “conductivity-building” hopping event. Points closer to the lower right corner of the plot correspond to states of lower hopping reversibility. Interestingly, the best performers happen to be the two most decoupled materials, $\text{pBvIm}^+\text{-Cl}^-$ and -TFSI^- .

Figure S25 makes it unclear whether this lower reversibility completely explains the improvement over AlCl_4^- for TFSI^- and Cl^- . If the ratio τ_S/τ_C is used to scale the total hopping frequency, then a modified frequency can be obtained, representing the frequency of conductivity-building hopping events. For a hypothetical decoupled material, such a value would be directly proportional to conductivity in systems with similar polymer dy-

namics. Figure S26 plots this modified hopping frequency against T_g/T . This graph bears

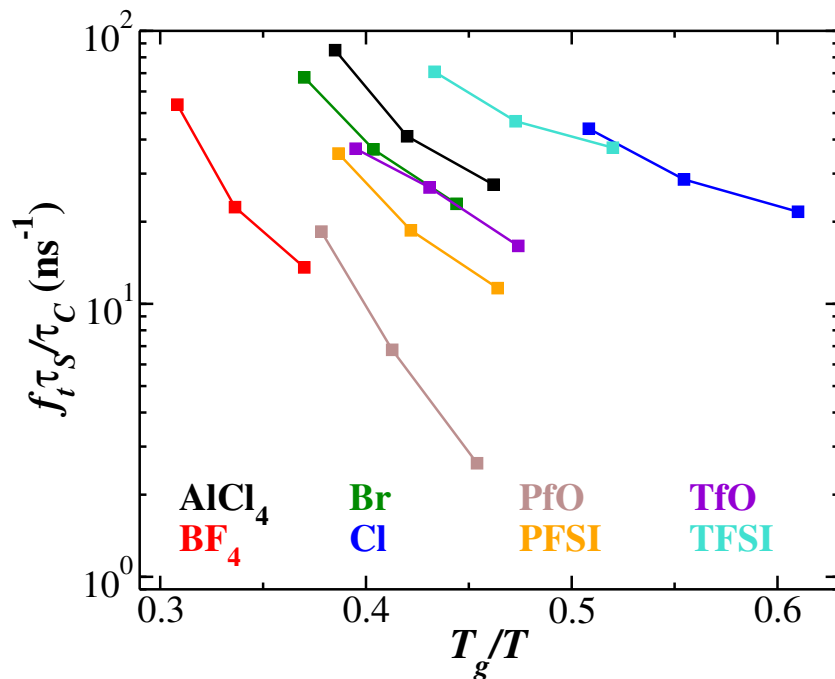


Figure S26: Comparison of the modified hopping frequency over inverse glass-transition-normalized temperature for all species in this study, where f_t is modified by the ratio τ_C/τ_S , representing the number of conduction hopping events.

remarkable similarity to Figure 2, confirming the influence of modified hopping frequency on conductivity. The overlapping Cl^- and TFSI^- curves in Figure S26 suggest that, despite the dissimilarity of these ions, their ion hopping dynamics are equivalent. Furthermore, the shallow slope for these two ions indicates that their hopping frequency is less responsive to changes in temperature, consistent with increased decoupling.

This qualitatively suggests that polymer segmental dynamics plays an important role in the ion hopping mechanism for some systems, and less important role in others, leading to the differences in decoupling phenomena observed in this study. Materials such as $\text{pBvIm}^+ \text{BF}_4^-$ and $\text{pBvIm}^+ \text{PfO}^-$ rely on segmental motion to open sufficient gaps in the polymer matrix for diffusion of the anion. In contrast, the large trough in the cation-cation $g(r)$ for $\text{pBvIm}^+ \text{AlCl}_4^-$ in Figure S21(a) must represent a sufficiently porous polymer matrix that permits

substantial diffusion without the aid of segmental motion. The pBvIm⁺-TFSI⁻ shares a similar $g(r)$ profile with -AlCl₄⁻, with two factors potentially responsible for improved conductivity: a smaller diffusion radius for TFSI⁻ and a smearing of charge over two halves of the molecule, reducing electrostatic binding energy. While Cl⁻, the smallest ion in this study, matches expectations as the most decoupled material,^{S46} it is still noteworthy that its dense polymer matrix permits ion hopping without substantial polymer rearrangement.

S3.6 Degree of decoupling

A recent study by Wojnarowska et al. summarized the state of the art in quantifying conductivity and segmental-dynamics decoupling.^{S47} When molar conductivity is 10⁻¹⁵ S/cm at T_g , charge transport in a material is said to be perfectly coupled to structural relaxation dynamics.^{S48,S49} Measuring such a quantity would allow us to utilize a decoupling index (R_σ) such as $R_\sigma(T_g) = 15 + \log(\sigma_{dc}(T_g))$.^{S50,S51} Unfortunately, such a measure is intractable for atomistic MD simulations near T_g . Alternatively, one can quantify temperature-dependent coupling by analyzing the proportionality between $\sigma_{dc}T$ and the structural relaxation time extracted from rheology.^{S47} This relationship is expressed as follows,

$$\frac{(\sigma T)^{-1}}{\tau} \propto \tau^{-\epsilon}, \quad (\text{S19})$$

with many studies having quantified the degree of decoupling using the ϵ parameter.^{S49,S52-S54} An $\epsilon > 0$ places a material in the superionic regime, and higher ϵ corresponds with higher degree of decoupling from structural dynamics.^{S47} Due to the long timescale for structural relaxations, it is impractical to extract the timescale from rheology using atomistic MD simulations. Instead, we can apply the timescale for ion-association relaxations, which contains contributions from both polymer-segmental and ion-relay dynamics.

Agapov et al. and Wang et al. demonstrated a correlation between chain rigidity (pro-

portional to the fragility) and the degree of decoupling.^{S52,S53} Agapov postulated that ions in high fragility polymers “move easily through the loose structure even when segmental relaxation is slow...”^{S52} Sangoro et al. and Wojnarowska et al. later concluded that frustrated chain packing increases free volume available through which conducting ions might move without the influence of polymer backbone motion.^{S47,S54} Wojnarowska et al. also touted this theory that the degree of decoupling increases with increasing chain rigidity.^{S47} However, through coarse-grained and atomistic MD simulations of polyILs, Simmons and coworkers cast doubt on the influence of fragility on degree of decoupling.^{S46} They reported new evidence linking ion size with degree of decoupling.^{S46} Specifically, their coarse-grained simulations revealed high sensitivity of degree of decoupling on free ion size and ion aggregation.^{S46} These observations are qualitatively consistent with the experimental results reported by Winey and coworkers on TAC⁺-Cl⁻, despite differences in these authors’ interpretation of the underlying mechanism.^{S55} While Simmons attributed lower T_g to the improved conductivity for the large polymerized ions, Winey focused on the influence of charge delocalization on ion hopping.

Another approach to quantifying the degree of decoupling involves capturing the activation energy of σ_{dc} by fitting the Arrhenius equation above T_g .^{S47} The dc conductivity is generally modeled using the relationship

$$\sigma_{dc}(T < T_g) = e\mu_{\infty}p_{\infty} \exp\left(\frac{-DT_0}{T - T_0}\right) \exp\left(\frac{-E_a^p}{RT}\right), \quad (\text{S20})$$

which includes the high-temperature limits of the number density of simultaneously conducting ions (p_{∞}) and mobility (μ_{∞}), the strength parameter D (related to the inverse of fragility), and the Vogel temperature T_0 .^{S56,S57} The first exponential, the Vogel-Fulcher-Tamman (VFT) temperature dependence, is associated with the mobility,^{S56–S60} while the Arrhenius term is derived from the conducting ion density.^{S56} As such, the activation energy

of the conducting ion density can be understood as the energy barrier for ion hopping, while the VFT form of mobility has been described as a reflection of the “coupling of segmental motion of polymer backbone and ion motion.”^{S56} Nakamura and coworkers described VFT temperature dependence at elevated temperature, transitioning to Arrhenius as temperature decreases for rigid (1-ethyl-3-vinylimidazolium)-based polyILs.^{S61} In fact, such behavior is often cited as typical for a superionic conductor; one whose ionic motion is decoupled from polymer dynamics.^{S62}

Since T_g captures polymer segmental relaxation rates in a convenient form, a natural expression of decoupling may be the thermal activation energy of conductivity as a function of temperature near T_g . Winey and coworkers, as discussed previously, show the conductivity logarithm of $[\text{TAC}]^+\text{-Cl}^-$ exhibiting a less negative slope versus inverse temperature compared to $[\text{TAC}]^+\text{-TFSI}^-$, consistent with a lower activation energy barrier.^{S55} Colby and coworkers showed that short-linker polyILs have a lower activation energy for conductivity,^{S57} suggesting that long linker segments should be avoided if one seeks good decoupling behavior. Removing this degree of freedom for material design could induce discovery of a predictable counterion-size effect and eliminate the confusion caused by the results of Chen et al. and similar studies due to their inclusion of long alkoxy- or similar linkers.^{S63} Additionally, to avoid uncertainties in the impact of finite diffusion length in spherical nanoparticles on dielectric response measurements, such as those found in the ER response study of Dong et al.,^{S64} we further winnow the relevant experimental evidence to that of membranes or other materials that can be safely assumed to be continuous at the nanoscale.

Can we extract an extent of decoupling from the correlation between ion-association structural relaxation time and conductivity? One can quantify temperature-dependent coupling by extracting the power-law exponent (ϵ) relating conductivity (σ), absolute temperature (T), and the inverse structural relaxation time (τ) extracted from rheology.^{S47,S52,S53} An $\epsilon > 0$ places a material in the superionic regime, and higher ϵ corresponds with higher degree of

decoupling to structural dynamics.^{S47} While we cannot access the structural relaxation time from rheology from MD simulations, we begin by substituting the ion-association counterpart (τ_C).

While diffusivity theoretically correlates with τ_C for polyILs, where the tethered ion is mostly immobile, this correlation is unfounded for ILs with dual mobile ions as seen in equation S7. Therefore, we need conductivity to extract a true degree of decoupling.

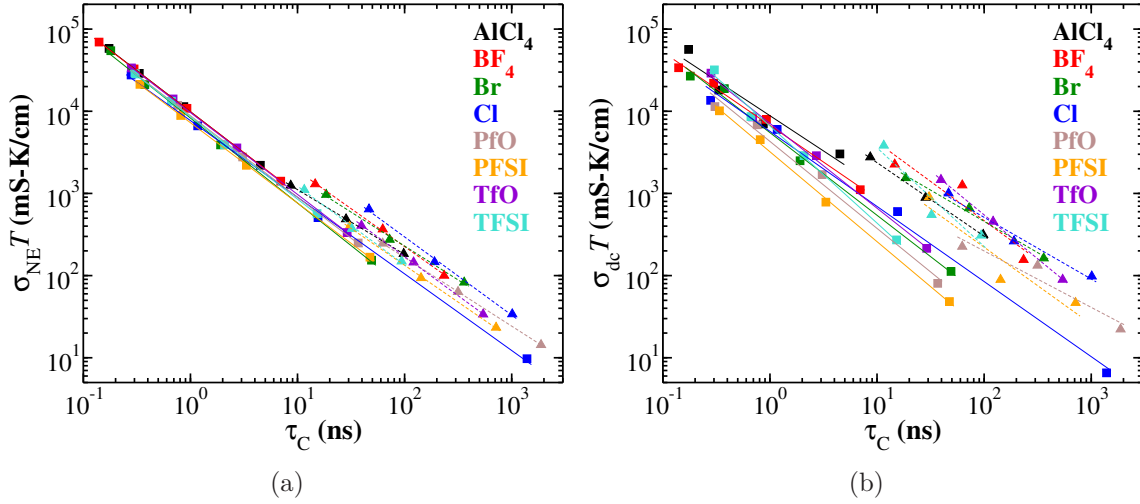


Figure S27: (a) Nernst-Einstein conductivity and (b) dc conductivity versus τ_C for all systems, with solid fitting lines for comparison.

Figure S27 shows the Nernst-Einstein and dc conductivities inserted in equation S19 and plotted against ion-association relaxation time. We switch from the degree of decoupling ϵ to the degree of coupling $1 - \epsilon$ to keep all values positive for Figure S28. Comparing the idealized Nernst-Einstein case against the true dc conductivity, it is clear that we will be unable to draw solid conclusions about degree of coupling from the analysis of true dc conductivity due to large errors. Figure S27(b) shows values for $1 - \epsilon$ extracted from the dc conductivity in Figure S27(b) for ILs (left bar) and polyILs (right bar). Results are mixed, and errors were not directly computed but are clearly very large by visual inspection of Figure S27(b), especially when rationalized in connection with the inherent uncertainties in

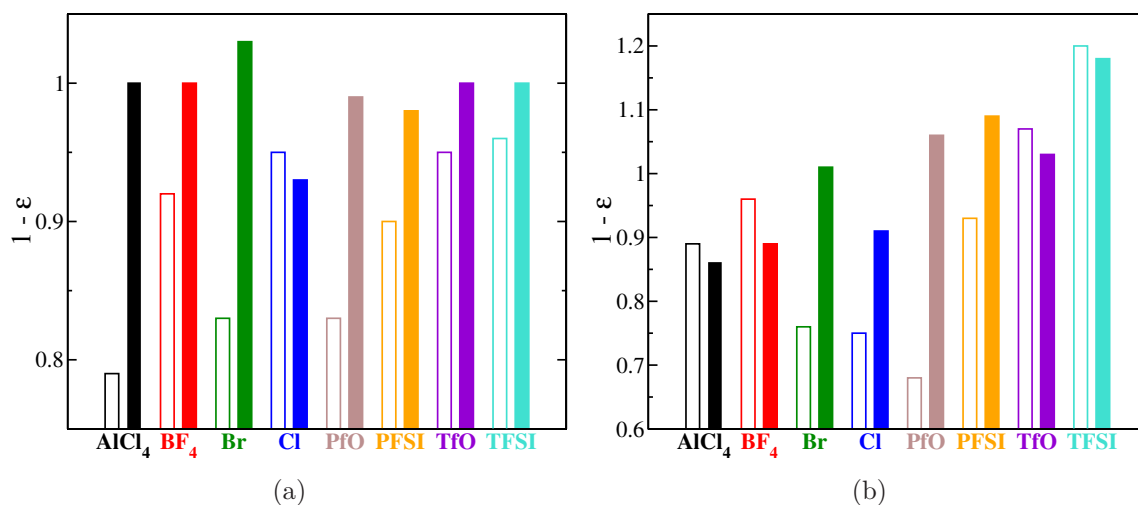


Figure S28: Degree of decoupling (ϵ) values for each counterion IL (filled symbols) and polyIL (open symbols) for (a) Nernst-Einstein conductivity and (b) dc conductivity.

the dc conductivity. The Nernst-Einstein representation in Figure S27(a) gives us a glimpse of decoupling effects possibly induced by polymerization. Specifically, all IL $(1 - \epsilon)$ values are within 7% of unity, suggesting that conductivity is perfectly coupled to structural relaxation, without regard to the counterion. If σ_{dc}/σ_{NE} holds constant for all temperatures, then this trend will hold for dc conductivity as well. All polyILs have $(1 - \epsilon)$ values less than unity, with no obvious trends due to ion size or other significant measures.

References

- (S1) Dommert, F.; Wendler, K.; Berger, R.; Delle Site, L.; Holm, C. Force fields for studying the structure and dynamics of ionic liquids: A critical review of recent developments. *ChemPhysChem* **2012**, *13*, 1625–1637.
- (S2) Morrow, T. I.; Maginn, E. J. Molecular Dynamics Study of the Ionic Liquid 1- n - Butyl-3-methylimidazolium Hexafluorophosphate. *The Journal of Physical Chemistry B* **2002**, *106*, 12807–12813.

- (S3) Bhargava, B. L.; Balasubramanian, S. Refined potential model for atomistic simulations of ionic liquid [bmim][PF6]. *The Journal of Chemical Physics* **2007**, *127*, 114510.
- (S4) Liu, H.; Maginn, E. A molecular dynamics investigation of the structural and dynamic properties of the ionic liquid 1-n-butyl-3-methylimidazolium bis (trifluoromethanesulfonyl) imide A molecular dynamics investigation of the structural and dynamic properties of the ionic l. *J. Chem. Phys* **2011**, *135*, 124507.
- (S5) Chaban, V. V.; Voroshylova, I. V.; Kalugin, O. N. A new force field model for the simulation of transport properties of imidazolium-based ionic liquids. *Phys Chem Chem Phys* **2011**, *13*, 7910–7920.
- (S6) Zhang, Y.; Maginn, E. J. A simple AIMD approach to derive atomic charges for condensed phase simulation of ionic liquids. *Journal of Physical Chemistry B* **2012**, *116*, 10036–10048.
- (S7) Sprenger, K. G.; Jaeger, V. W.; Pfaendtner, J. The general AMBER force field (GAFF) can accurately predict thermodynamic and transport properties of many ionic liquids. *Journal of Physical Chemistry B* **2015**, *119*, 5882–5895.
- (S8) Zhang, Y.; Maginn, E. J. Direct Correlation between Ionic Liquid Transport Properties and Ion Pair Lifetimes: A Molecular Dynamics Study. *The Journal of Physical Chemistry Letters* **2015**, *705*, 700–705.
- (S9) Mogurampelly, S.; Keith, J. R.; Ganesan, V. Mechanisms Underlying Ion Transport in Polymerized Ionic Liquids. *Journal of the American Chemical Society* **2017**, *139*, 9511–9514.
- (S10) Keith, J.; Mogurampelly, S.; Aldukhi, F.; Wheatle, B.; Ganesan, V. Influence of molecular weight on ion-transport properties of polymeric ionic liquids. *Phys Chem Chem Phys* **2017**, *19*, 29134.

- (S11) Keith, J. R.; Mogurampelly, S.; Wheatle, B. K.; Ganesan, V. Influence of side chain linker length on ion-transport properties of polymeric ionic liquids. *Journal of Polymer Science Part B: Polymer Physics* **2017**, *55*, 1718–1723.
- (S12) Frisch, M. J.; Trucks, G. W.; Schlegel, H. B.; Scuseria, G. E.; Robb, M. A.; Cheeseman, J. R.; Scalmani, G.; Barone, V.; Petersson, G. A.; Nakatsuji, H.; Li, X.; Caricato, M.; Marenich, A. V.; Bloino, J.; Janesko, B. G.; Gomperts, R.; Menucci, B.; Hratchian, H. P.; Ortiz, J.; Izmaylov, A. F.; Sonnenberg, J. L.; Williams-Young, D.; Ding, F.; Lipparini, F.; Egidi, F.; Goings, J.; Peng, B.; Petrone, A.; Henderson, T.; Ranasinghe, D.; Zakrzewski, V. G.; Gao, J.; Rega, N.; Zheng, G.; Liang, W.; Hada, M.; Ehara, M.; Toyota, K.; Fukuda, R.; Hasegawa, J.; Ishida, M.; Nakajima, T.; Honda, Y.; Kitao, O.; Nakai, H.; Vreven, T.; Throssell, K.; Montgomery, Jr., J. A.; Peralta, J. E.; Ogliaro, F.; Bearpark, M. J.; Heyd, J. J.; Brothers, E. N.; Kudin, K. N.; Staroverov, V. N.; Keith, T. A.; Kobayashi, R.; Normand, J.; Fox, D. J. Gaussian 16. 2016.
- (S13) Singh, U. C.; Kollman, P. A. An approach to computing electrostatic charges for molecules. *J. Comput. Chem.* **1984**, *5*, 129–145.
- (S14) Besler, B. H.; Merz, K. M.; Kollman, P. A. Atomic charges derived from semiempirical methods. *J. Comput. Chem.* **1990**, *11*, 431–439.
- (S15) Wang, J. M.; Wolf, R. M.; Caldwell, J. W.; Kollman, P. A.; Case, D. A. Development and testing of a general amber force field. *J. Comput. Chem.* **2004**, *25*, 1157–1174.
- (S16) Wang, J.; Wang, W.; Kollman, P. A.; Case, D. A. Automatic atom type and bond type perception in molecular mechanical calculations. *Journal of Molecular Graphics and Modelling* **2006**, *25*, 247–260.

- (S17) Martinez, L.; Andrade, R.; Birgin, E.; Martinez, J. Packmol: A Package for Building Initial Configurations for Molecular Dynamics Simulations. *Journal of computational chemistry* **2009**, *30*, 2157–2164.
- (S18) Schneider, T.; Stoll, E. Molecular-dynamics study of a three-dimensional one-component model for distortive phase transitions. *Physical Review B* **1978**, *17*, 1302–1322.
- (S19) Berendsen, H. J.; Postma, J. P.; Van Gunsteren, W. F.; Dinola, A.; Haak, J. R. Molecular dynamics with coupling to an external bath. *The Journal of Chemical Physics* **1984**, *81*, 3684–3690.
- (S20) Plimpton, S. Fast Parallel Algorithms for Short-Range Molecular Dynamics. *Journal of Computational Physics* **1995**, *117*, 1–19.
- (S21) Sun, H. COMPASS: An ab Initio Force-Field Optimized for Condensed-Phase Applications Overview with Details on Alkane and Benzene Compounds. *The Journal of Physical Chemistry B* **1998**, *102*, 7338–7364.
- (S22) Hockney, R.; Eastwood, J. *Computer Simulation Using Particles*; CRC Press, 1988.
- (S23) Plimpton, S.; Pollock, R.; Stevens, M. J. Particle Mesh Ewald and rRESPA for Parallel Molecular Dynamics Simulations. Proceedings of the Eighth Siam Conference on Parallel Processing for Scientific Computing. 1997; pp 1–13.
- (S24) Shinoda, W.; Shiga, M.; Mikami, M. Rapid estimation of elastic constants by molecular dynamics simulation under constant stress. *Physical Review B - Condensed Matter and Materials Physics* **2004**, *69*, 134103.
- (S25) Martyna, G. J.; Tobias, D. J.; Klein, M. L. Constant pressure molecular dynamics algorithms. *The Journal of Chemical Physics* **1994**, *101*, 4177–4189.

- (S26) Parrinello, M.; Rahman, A. Polymorphic transitions in single crystals: A new molecular dynamics method. *Journal of Applied Physics* **1981**, *52*, 7182–7190.
- (S27) Tuckerman, M. E.; Alejandre, J.; López-Rendón, R.; Jochim, A. L.; Martyna, G. J. A Liouville-operator derived measure-preserving integrator for molecular dynamics simulations in the isothermal–isobaric ensemble. *Journal of Physics A: Mathematical and General* **2006**, *39*, 5629–5651.
- (S28) Jorgensen, W. L.; Maxwell, D. S.; Tirado-Rives, J. Development and Testing of the OLPS All-Atom Force Field on Conformational Energetics and Properties of Organic Liquids. *J. Am. Chem. Soc.* **1996**, *118*, 11225–11236.
- (S29) Sambasivarao, S. V.; Acevedo, O. Development of OPLS-AA force field parameters for 68 unique ionic liquids. *Journal of Chemical Theory and Computation* **2009**, *5*, 1038–1050.
- (S30) De Andrade, J.; Böes, E. S.; Stassen, H. Computational study of room temperature molten salts composed by 1-alkyl-3-methylimidazolium cations - Force-field proposal and validation. *Journal of Physical Chemistry B* **2002**, *106*, 13344–13351.
- (S31) Urahata, S. M.; Ribeiro, M. C. C. Single particle dynamics in ionic liquids of 1-alkyl-3-methylimidazolium cations. *Journal of Chemical Physics* **2005**, *122*, 1–10.
- (S32) Canongia Lopes, J. N.; Deschamps, J.; Pádua, A. a. H. Modeling Ionic Liquids Using a Systematic All-Atom Force Field. *Journal of Physical Chemistry B* **2004**, *108*, 2038–2047.
- (S33) Lopes, J. N.; Pádua, A. A. Molecular force field for ionic liquids composed of triflate or bistriflylimide anions. *Journal of Physical Chemistry B* **2004**, *108*, 16893–16898.

- (S34) Tsuzuki, S.; Shinoda, W.; Saito, H.; Mikami, M.; Tokuda, H.; Watanabe, M. Molecular dynamics simulations of ionic liquids: Cation and anion dependence of self-diffusion coefficients of ions. *Journal of Physical Chemistry B* **2009**, *113*, 10641–10649.
- (S35) Green, M. D.; Salas-De La Cruz, D.; Ye, Y.; Layman, J. M.; Elabd, Y. A.; Winey, K. I.; Long, T. E. Alkyl-substituted N-vinylimidazolium polymerized ionic liquids: Thermal properties and ionic conductivities. *Macromolecular Chemistry and Physics* **2011**, *212*, 2522–2528.
- (S36) Bocharova, V.; Wojnarowska, Z.; Cao, P. F.; Fu, Y.; Kumar, R.; Li, B.; Novikov, V. N.; Zhao, S.; Kisliuk, A.; Saito, T.; Mays, J. W.; Sumpter, B. G.; Sokolov, A. P. Influence of Chain Rigidity and Dielectric Constant on the Glass Transition Temperature in Polymerized Ionic Liquids. *Journal of Physical Chemistry B* **2017**, *121*, 11511–11519.
- (S37) Ueberreiter, K.; Kanig, G. Self-plasticization of polymers. *Journal of Colloid Science* **1952**, *7*, 569–583.
- (S38) Iacob, C.; Matsumoto, A.; Brennan, M.; Liu, H.; Paddison, S. J.; Urakawa, O.; Inoue, T.; Sangoro, J.; Runt, J. Polymerized Ionic Liquids: Correlation of Ionic Conductivity with Nanoscale Morphology and Counterion Volume. *ACS Macro Letters* **2017**, *6*, 941–946.
- (S39) Nakamura, K.; Fukao, K.; Inoue, T. Dielectric relaxation and viscoelastic behavior of polymerized ionic liquids with various counteranions. *Macromolecules* **2012**, *45*, 3850–3858.
- (S40) Slattery, J. M.; Daguenet, C.; Dyson, P. J.; Schubert, T. J.; Krossing, I. How to predict the physical properties of ionic liquids: A volume-based approach. *Angewandte Chemie - International Edition* **2007**, *46*, 5384–5388.

- (S41) Beichel, W.; Preiss, U. P.; Verevkin, S. P.; Koslowski, T.; Krossing, I. Empirical description and prediction of ionic liquids' properties with augmented volume-based thermodynamics. *Journal of Molecular Liquids* **2014**, *192*, 3–8.
- (S42) Marcus, Y. Ionic and molar volumes of room temperature ionic liquids. *Journal of Molecular Liquids* **2015**, *209*, 289–293.
- (S43) Jenkins, H. D. B.; Roobottom, H. K.; Passmore, J.; Glasser, L. Relationships among Ionic Lattice Energies, Molecular (Formula Unit) Volumes, and Thermochemical Radii. *Inorganic Chemistry* **1999**, *38*, 3609–3620.
- (S44) Heres, M.; Cosby, T.; Mapesa, E. U.; Liu, H.; Berdzinski, S.; Strehmel, V.; Dadmun, M.; Paddison, S. J.; Sangoro, J. Ion Transport in Glassy Polymerized Ionic Liquids: Unraveling the Impact of the Molecular Structure. *Macromolecules* **2019**, *52*, 88–95.
- (S45) Mogurampelly, S.; Ganesan, V. Ion Transport in Polymerized Ionic Liquid–Ionic Liquid Blends. *Macromolecules* **2018**, *51*, acs.macromol.8b01460.
- (S46) Cheng, Y.; Yang, J.; Hung, J.-H.; Patra, T. K.; Simmons, D. S. Design Rules for Highly Conductive Polymeric Ionic Liquids from Molecular Dynamics Simulations. *Macromolecules* **2018**,
- (S47) Wojnarowska, Z.; Feng, H.; Fu, Y.; Cheng, S.; Carroll, B.; Kumar, R.; Novikov, V. N.; Kisliuk, A. M.; Saito, T.; Kang, N.-G.; Mays, J. W.; Sokolov, A. P.; Bocharova, V. Effect of Chain Rigidity on the Decoupling of Ion Motion from Segmental Relaxation in Polymerized Ionic Liquids: Ambient and Elevated Pressure Studies. *Macromolecules* **2017**, acs.macromol.7b01217.
- (S48) Mizuno, F.; Belieres, J. P.; Kuwata, N.; Pradel, A.; Ribes, M.; Angell, C. A. Highly decoupled ionic and protonic solid electrolyte systems, in relation to other relaxing

- systems and their energy landscapes. *Journal of Non-Crystalline Solids* **2006**, *352*, 5147–5155.
- (S49) Choi, U. H.; Mittal, A.; Price, T. L.; Lee, M.; Gibson, H. W.; Runt, J.; Colby, R. H. Molecular Volume Effects on the Dynamics of Polymerized Ionic Liquids and their Monomers. *Electrochimica Acta* **2015**, *175*, 55–61.
- (S50) Angell, C. Fast ion motion in glassy and amorphous materials. *Solid State Ionics* **1983**, *9-10*, 3–16.
- (S51) Ingram, M. D. Ionic conductivity and glass structure. *Philosophical Magazine B* **1989**, *60*, 729–740.
- (S52) Agapov, A. L.; Sokolov, A. P. Decoupling ionic conductivity from structural relaxation: A way to solid polymer electrolytes? *Macromolecules* **2011**, *44*, 4410–4414.
- (S53) Wang, Y.; Agapov, A. L.; Fan, F.; Hong, K.; Yu, X.; Mays, J.; Sokolov, A. P. Decoupling of ionic transport from segmental relaxation in polymer electrolytes. *Physical Review Letters* **2012**, *108*, 1–5.
- (S54) Sangoro, J. R.; Iacob, C.; Agapov, A. L.; Wang, Y.; Berdzinski, S.; Rexhausen, H.; Strehmel, V.; Friedrich, C.; Sokolov, A. P.; Kremer, F. Decoupling of ionic conductivity from structural dynamics in polymerized ionic liquids. *Soft Matter* **2014**, *10*, 3536–3540.
- (S55) Griffin, P. J.; Freyer, J. L.; Han, N.; Geller, N.; Yin, X.; Gheewala, C. D.; Lambert, T. H.; Campos, L. M.; Winey, K. I. Ion Transport in Cyclopropenium-Based Polymerized Ionic Liquids. *Macromolecules* **2018**, acs.macromol.7b02546.
- (S56) Lee, M.; Choi, U. H.; Colby, R. H.; Gibson, H. W. Ion conduction in imidazolium

- acrylate ionic liquids and their polymers. *Chemistry of Materials* **2010**, *22*, 5814–5822.
- (S57) Choi, U. H.; Ye, Y.; Salas De La Cruz, D.; Liu, W.; Winey, K. I.; Elabd, Y. A.; Runt, J.; Colby, R. H. Dielectric and viscoelastic responses of imidazolium-based ionomers with different counterions and side chain lengths. *Macromolecules* **2014**, *47*, 777–790.
- (S58) Macdonald, J. R. Theory of ac space-charge polarization effects in photoconductors, semiconductors, and electrolytes. *Physical Review* **1953**, *92*, 4–17.
- (S59) Macdonald, J. R. Simplified impedance-frequency-response results for intrinsically conducting solids and liquids. *The Journal of Chemical Physics* **1974**, *61*, 3977–3996.
- (S60) Klein, R. J.; Zhang, S.; Dou, S.; Jones, B. H.; Colby, R. H.; Runt, J. Modeling electrode polarization in dielectric spectroscopy: Ion mobility and mobile ion concentration of single-ion polymer electrolytes. *Journal of Chemical Physics* **2006**, *124*, 144903.
- (S61) Nakamura, K.; Saiwaki, T.; Fukao, K. Dielectric relaxation behavior of polymerized ionic liquid. *Macromolecules* **2010**, *43*, 6092–6098.
- (S62) Agrawal, R. C.; Gupta, R. K. Superionic solids: composite electrolyte phase - an overview. *Journal of Materials Science* **1999**, *34*, 1131–1162.
- (S63) Chen, M.; Dugger, J. W.; Li, X.; Wang, Y.; Kumar, R.; Meek, K. M.; Uhrig, D. W.; Browning, J. F.; Madsen, L. A.; Long, T. E.; Lokitz, B. S. Polymerized ionic liquids: Effects of counter-anions on ion conduction and polymerization kinetics. *Journal of Polymer Science Part A: Polymer Chemistry* **2018**, 1346–1357.
- (S64) Dong, Y.; Liu, Y.; Wang, B.; Xiang, L.; Zhao, X.; Yin, J. Influence of counterion type

on dielectric and electrorheological responses of poly(ionic liquid)s. *Polymer (United Kingdom)* **2017**, *132*, 273–285.